

BIOMIMETICS

An organosynthetic dynamic heart model with enhanced biomimicry guided by cardiac diffusion tensor imaging

Clara Park¹, Yiling Fan^{1,2}, Gregor Hager^{3,4}, Hyunwoo Yuk¹, Manisha Singh^{3,5}, Allison Rojas³, Aamir Hameed^{6,7}, Mossab Saeed^{2,8}, Nikolay V. Vasilyev^{2,8}, Terry W. J. Steele^{5,9}, Xuanhe Zhao^{1,10}, Christopher T. Nguyen^{2,11,12*†}, Ellen T. Roche^{1,2,3*†}

The complex motion of the beating heart is accomplished by the spatial arrangement of contracting cardiomyocytes with varying orientation across the transmural layers, which is difficult to imitate in organic or synthetic models. High-fidelity testing of intracardiac devices requires anthropomorphic, dynamic cardiac models that represent this complex motion while maintaining the intricate anatomical structures inside the heart. In this work, we introduce a biorobotic hybrid heart that preserves organic intracardiac structures and mimics cardiac motion by replicating the cardiac myofiber architecture of the left ventricle. The heart model is composed of organic endocardial tissue from a preserved explanted heart with intact intracardiac structures and an active synthetic myocardium that drives the motion of the heart. Inspired by the helical ventricular myocardial band theory, we used diffusion tensor magnetic resonance imaging and tractography of an unraveled organic myocardial band to guide the design of individual soft robotic actuators in a synthetic myocardial band. The active soft tissue mimic was adhered to the organic endocardial tissue in a helical fashion using a custom-designed adhesive to form a flexible, conformable, and watertight organosynthetic interface. The resulting biorobotic hybrid heart simulates the contractile motion of the native heart, compared with in vivo and in silico heart models. In summary, we demonstrate a unique approach fabricating a biomimetic heart model with faithful representation of cardiac motion and endocardial tissue anatomy. These innovations represent important advances toward the unmet need for a high-fidelity in vitro cardiac simulator for preclinical testing of intracardiac devices.

INTRODUCTION

There is an unmet clinical need for a high-fidelity benchtop cardiac model for device testing, interventional training, and procedure demonstration. Currently, in most in vitro cardiac simulators, the heart is represented by entirely synthetic or entirely organic components (1–4). Although synthetic hearts, which are typically silicone- or urethane-based anatomical models, have utility for well-regulated, repeatable experimental conditions, their biofidelity is limited owing to a lack of correct intracardiac anatomical details necessary for evaluating the function and simulating the placement of intracardiac devices (such as transcatheter valve replacements or occluder devices). Although a realistic representation of cardiac anatomy is achievable by using ex vivo beating heart models (5–7), the setup process can be long and tedious, and the ex vivo heart tissue has

limited longevity (<1 day) due to muscle stiffening and decay. Owing to these drawbacks, in vivo animal models are commonly used in industry to test the mechanical performance of intracardiac devices, involving substantial experimental cost and time.

The heart is a uniquely challenging organ to recreate due to its dynamic three-dimensional (3D) motion and its complex internal cardiac structures. Engineering approaches to making realistic beating heart models include the use of soft robotics and tissue engineering. Recent advances in soft robotics have demonstrated success in replicating complex biological motions at the macroscale (8–12). Our previous work (8) demonstrated physiological cardiac motion by programming linear pneumatic artificial muscles (PAMs) (13, 14) in a soft matrix. This simplified cardiac simulator, however, lacks anatomical intracardiac structures (such as papillary muscles, chordae tendineae, ventricular trabeculae, valves, and moderator bands). With varying mechanical properties and feature sizes, these structures are challenging to implement with currently available synthetic materials and manufacturing methods at the submillimeter resolution (15, 16). On the other hand, entirely biological approaches to recreating the heart in the field of cardiac tissue engineering range from using induced pluripotent stem cells (17) and bioprinting cell-seeded artificial scaffolds (18, 19) to decellularized heart tissues (20). However, currently, there is no functional bioartificial heart at the human organ scale. There are remaining challenges in scaling up tissue-engineered constructs due to difficulties in obtaining cells and sustaining tissue vascularization and viability (21), as well as in achieving the contractile function at a physiological level even at the microscale. Furthermore, the use of viable biological tissues requires the maintenance of sterile culture conditions at all times, making it impractical for benchtop testing.

¹Department of Mechanical Engineering, Massachusetts Institute of Technology, Cambridge, MA, USA. ²Harvard Medical School, Boston, MA, USA. ³Institute for Medical Engineering and Science, Massachusetts Institute of Technology, Cambridge, MA, USA. ⁴Department of Mechanical Engineering, Technical University of Munich, Munich, Germany. ⁵NTU-Northwestern Institute for Nanomedicine, Interdisciplinary Graduate School, Nanyang Technological University, Singapore, Singapore. ⁶Tissue Engineering Research Group, Department of Anatomy, Royal College of Surgeons in Ireland, Dublin, Ireland. ⁷Trinity Centre for Biomedical Engineering, Trinity College Dublin, Dublin, Ireland. ⁸Department of Cardiac Surgery, Boston Children's Hospital, Boston, MA, USA. ⁹School of Materials Science and Engineering, Nanyang Technological University, Singapore, Singapore. ¹⁰Department of Civil and Environmental Engineering, Massachusetts Institute of Technology, Cambridge, MA, USA. ¹¹Martinos Center for Biomedical Imaging, Massachusetts General Hospital, Charlestown, MA, USA. ¹²Cardiovascular Research Center, Massachusetts General Hospital, Charlestown, MA, USA.

*These authors contributed equally to this work.

†Corresponding author. Email: christopher.nguyen@mgh.harvard.edu (C.T.N.); etr@mit.edu (E.T.R.)

Motivated by the lack of a synthetic or biological method to recapitulate both the complex motion and anatomical features of the heart, we present a biohybrid approach that combines organic and synthetic components. We propose using endocardial (inner heart) tissue directly from a porcine heart to accurately represent the anatomical details of intracardiac structures while using soft robotic techniques to recreate the dynamic cardiac motion. Moreover, the heart tissue is chemically fixed to enhance longevity for benchtop settings. By using soft robotic techniques to replicate physiological motion and merging this technology with organic tissue, we can overcome both the scalability limitations in tissue engineering and the challenges in recreation of fine structural details with conventional manufacturing technology.

Specifically, in our approach to programming active synthetic muscles, we sought to mimic the intricate arrangements of cardiac fibers. The native myocardium (heart muscle) is composed of layers of individual cardiomyocyte fibers that synchronously contract along their transmurally varying orientations, constituting hierarchical 3D structures. Instead of replicating the complex fiber structures directly in 3D, we took inspiration from the helical ventricular myocardial band (HVMB) theory (22–25) to simplify the design and fabrication process of the soft robotic muscles. According to this theory, the ventricle of the heart can be unraveled into a singular muscular band that is spirally arranged in the 3D space. Here, we constructed a two-dimensional (2D) biomimetic matrix by embedding multiple linearly contracting PAMs in a soft matrix based on the fiber orientations of the flat unraveled heart. Then, the soft robotic matrix was rewrapped into a 3D shape to recreate the hierarchical, functional architecture and the global 3D motion of the ventricular myocardium.

As represented in Fig. 1, an explanted porcine heart was reconfigured so that the intact intracardiac structures (ex vivo endocardial scaffold) were preserved, but expired myocardial tissue was substituted with an actuable HVMB-inspired synthetic myocardium to restore the dynamic motion of the beating heart. We refer to this dynamic heart model as a biorobotic hybrid heart.

In the development of this biorobotic hybrid heart, we have made some important technological advancements. First, we described a method for constructing a biohybrid heart that consists of an ex vivo endocardial tissue scaffold and synthetic myocardium. Second, we developed a soft tissue silicone adhesive to allow coupling of the organic endocardium and synthetic myocardium, because existing adhesives suffer from critical drawbacks, such as weak adhesion (e.g., polyethylene glycol- or fibrin-based adhesives) between tissue and silicone, mechanical mismatch with soft tissues, brittleness, and incompatibility in wet environment [e.g., cyanoacrylates (CAs)] (26–28). Our novel adhesive forms a reliable organosynthetic interface while handling large deformations in wet conditions. Third, we developed a flat soft robotic matrix that contains an array of PAMs whose fine fiber reinforcement can be oriented to match the native heart tissue anisotropy. McKibben PAMs used in previous studies (8, 29) occupy high dead volume in unactuated state, which would limit the number of actuators that can fit in a confined space, such as the ventricular myocardium geometry. For enhanced biomimicry, we used flat pleated PAMs (fPAMs) (30, 31) with zero-volume air cavities in the unpressurized state to increase actuator multiplexity and resolution. We made an fPAM matrix that can be manufactured by a one-step fabrication process for a high degree of actuator multiplexity and seamlessly integrated into a soft tissue-mimicking

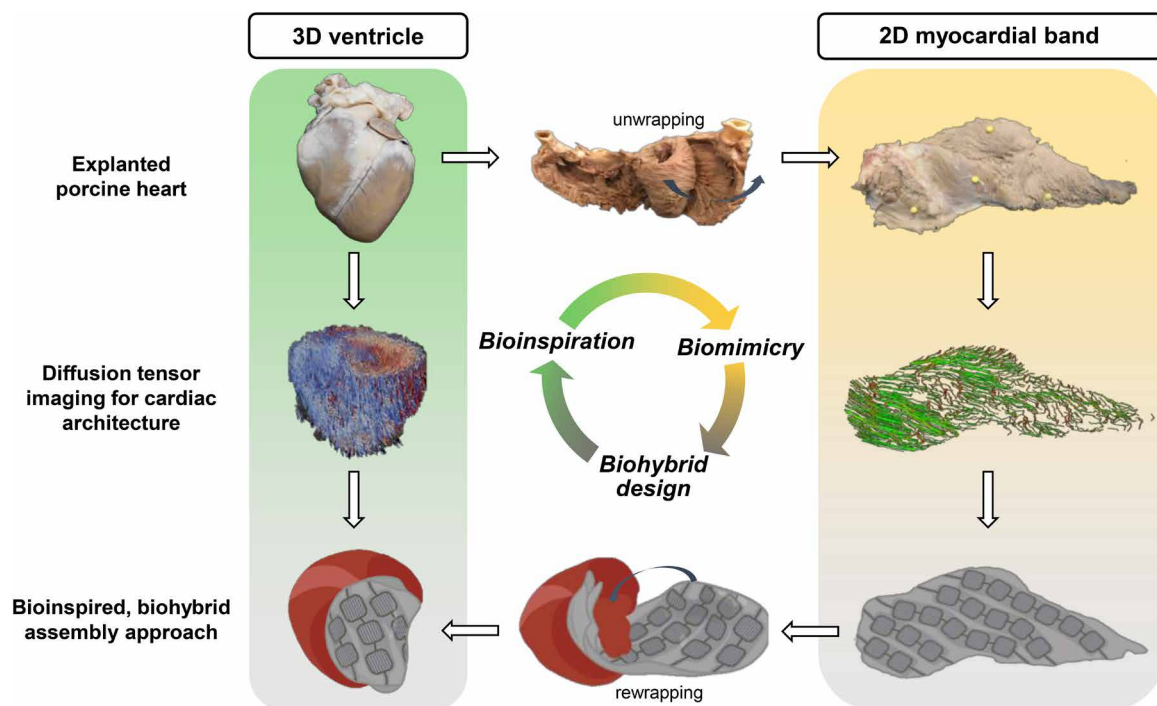


Fig. 1. Overview of the bioinspired approach to developing a biorobotic hybrid heart. An explanted porcine heart tissue was dissected and unraveled to form a flat HVMB. DT-MRI of the intact and unraveled heart was used to guide the development of a synthetic myocardial substitute. A 2D active band was designed on the basis of the unraveled heart cardiomyocyte orientation. The band was rewrapped around a preserved heart without myocardium, and the organic and synthetic structures were coupled to form a biorobotic hybrid heart.

material. Last, we introduced a method for translating high-resolution cardiac myofiber orientation architecture to soft robotic structures using diffusion tensor magnetic resonance imaging (DT-MRI), a nondestructive technique that reveals fiber architecture by detecting anisotropic diffusion of water in tissue (32–34). With the combination of these technologies, we demonstrate a platform for a dynamic heart model that is durable, is anatomically accurate, and can recapitulate physiological motion. In the future, this bio-robotic heart may be used as a high-fidelity cardiac benchtop model for the development of intracardiac devices, potentially reducing the overall number of animals used in preclinical and regulatory testing.

RESULTS

Construction of a passive biohybrid heart

First, we constructed a passive biohybrid heart with silicone as a myocardial substitute. A whole porcine heart was explanted and fixed with 10% formalin to prevent tissue decaying and extend longevity. The ventricular walls of the fixed heart tissue were then cast to create an outer mold (Fig. 2A). Subsequently, the left ventricular and interventricular septal myocardial tissue was removed by hand dissection, using the transmurally changing fiber orientation as the guide to inform the extent of removal through the muscle layers (Fig. 2B and see the “Ex vivo heart dissection” section in Materials and Methods). This dissection method removed the muscle from the left ventricular and interventricular septal tissues, leaving the endocardial tissue and its intracardiac structures intact (organic endocardial scaffold) (Fig. 2B).

Next, we constructed a synthetic myocardium from a soft silicone elastomer (Ecoflex 00-20, Smooth-On) that has a Young's modulus of 37.8 ± 1.84 kPa, which is within the range of fresh myocardial tissues in our uniaxial tensile tests (fig. S3) and corroborated by literature values (35–37). The synthetic myocardium was cast by pouring silicone into a mold assembly consisting of the outer mold (from Fig. 2A) and the endocardial scaffold (from Fig. 2B). This assembly is shown in Fig. 2C. Once the silicone myocardium was cast, the components were demolded and disassembled. Reassembly of the tissue structures and synthetic myocardium required a tissue/silicone adhesive.

Adhesion of tissue-silicone interface

To bond two dissimilar materials (fixed organic tissue and silicone myocardium), we developed a custom soft adhesive. Polydimethylsiloxane (PDMS) (Sylgard 184, Dow Corning) was chosen as the soft substrate for the adhesive layer at the interface because of its elasticity and its ability to readily integrate with other platinum-based silicones, such as Ecoflex. We developed a tissue-to-silicone adhesive called TissueSil, based on modifications of previously described chemistry (38–40). In TissueSil adhesive technology, triethoxy vinyl silane was introduced to covalently bond with siloxane cross-linkers available in the PDMS resin during Pt-catalyzed curing process, which functionalizes PDMS with triethoxy silane groups on the surface. Next, on the tissue, 3-(triethoxysilyl)propyl isocyanate was introduced to form covalent bonds with various functional groups—including nucleophiles (–Nu), hydroxyls (–OH), or primary amines (–NH₂) groups of the tissue—leaving triethoxy silane functional groups on the tissue surface (chemistry shown in fig. S1A). In the presence of water, ethoxy groups in silane functional groups can be hydrolyzed

into silanol (Si–OH) groups, generating ethanol as the reaction byproduct. When the silanol groups in tissue and PDMS are in physical contact, a condensation reaction occurs over time between two adjacent silanol groups and forms siloxane bonds with a generation of water as reaction byproduct. As a result, covalent coupling is formed between the PDMS and the tissue. TissueSil can be applied using two methods. Depending on the application, a premade silicone myocardium may be integrated with tissue in one step by coating tissue with TissueSil resin and assembling the two pieces. Alternatively, the silicone resin may be poured onto cured TissueSil that is coated on the tissue surface before integration.

To ensure the conformability of the adhesive to a rough tissue surface, we imaged the micromorphology of the tissue-adhesive interface using scanning electron microscopy (SEM). We demonstrated excellent conformability to the tissue surface (Fig. 3A), with interpenetration of TissueSil into the fixed myocardial tissue. To confirm conformability between the rough tissue surface and synthetic myocardium after assembling with the soft adhesive, we added barium sulfate to TissueSil and imaged a fully constructed biohybrid heart with microcomputed tomography (microCT) to visualize the applied adhesive between the tissue and interface (Fig. 3B). We observed excellent conformability between the tissue and the elastomeric substitute myocardium.

To evaluate the effect of TissueSil on tissue mechanical properties, we performed uniaxial tensile testing of fixed myocardial tissue coated with TissueSil and compared it with uncoated tissue, tissue/DuraSeal, and tissue/ethyl-based CA constructs (Fig. 4A). TissueSil and DuraSeal did not change the overall stiffness of fixed tissue, whereas the coating of CA contributed to a significant increase in the modulus. There was a premature failure of the CA layer, which cracked and eventually delaminated from the tissue surface (Fig. 4A and movie S1). Conversely, TissueSil and DuraSeal stretched with the tissue substrate without cracking or delaminating before tissue failure.

TissueSil and DuraSeal were evaluated for their ability to bond fixed myocardium to synthetic Ecoflex using lap shear, peel, tack adhesion, and burst pressure test methods. CA was excluded from this testing due to its inability to handle large strains, as seen in Fig. 4A and movie S1. In all cases (lap shear/peel/tack/burst), bonding with TissueSil required higher maximum load/stress at failure when compared with DuraSeal (Fig. 4, B to E). TissueSil provides 13 times higher peel force and 26 times stronger tack adhesion than commercially available DuraSeal sealant. TissueSil can also withstand physiological systolic pressure of up to 120 mmHg.

To test the durability of the organosynthetic interface, we performed a high-cycle fatigue test on the TissueSil/tissue composite with a strain of 15% at 1 Hz for 30,000 cycles. There was a very slow progression of adhesive delamination, as can be seen in the hysteresis loop and visual inspection (fig. S4, A and B). Conversely, the CA/tissue composite experienced an immediate cracking of the CA layer at its first cycle, demonstrating its incompatibility to handle dynamic physiological strain (fig. S4C).

Development and characterization of soft robotic cardiac muscles

To make a contractile synthetic myocardium, we chose to embed pneumatic actuators in the Ecoflex matrix. We customized fPAMs to minimize actuator thickness and therefore maximize the ability to mimic cardiomyocyte orientation. We developed a method to

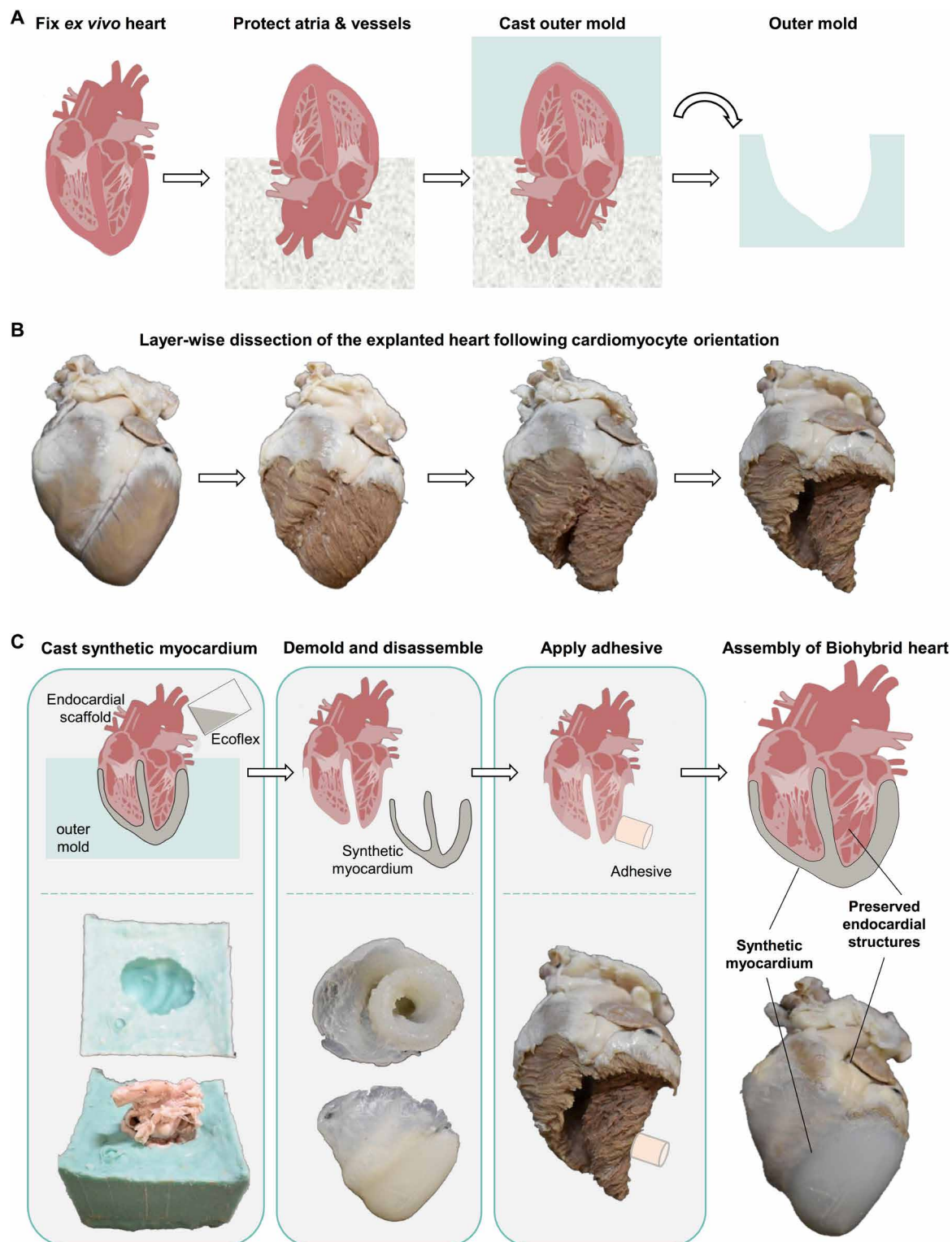


Fig. 2. Fabrication process for a passive biohybrid heart. (A) The outer mold was cast as shown. An explanted porcine heart was preserved, and the superior portion was placed in sulfur-free clay. The epicardial surface of the ventricular portion of the heart was then cast with Mold Star 15. (B) The preserved heart was dissected in a layer-wise fashion after the cardiomyocyte orientation in the left ventricle. (C) The passive biohybrid heart was cast by centering the dissected heart in the outer mold using supporting struts. Ecoflex 00-20 was used for casting. Once cured, the assembly was demolded and disassembled. Next, tissue-silicone adhesive (TissueSil) was applied to the outer tissue surface and reassembled to synthetic myocardium.

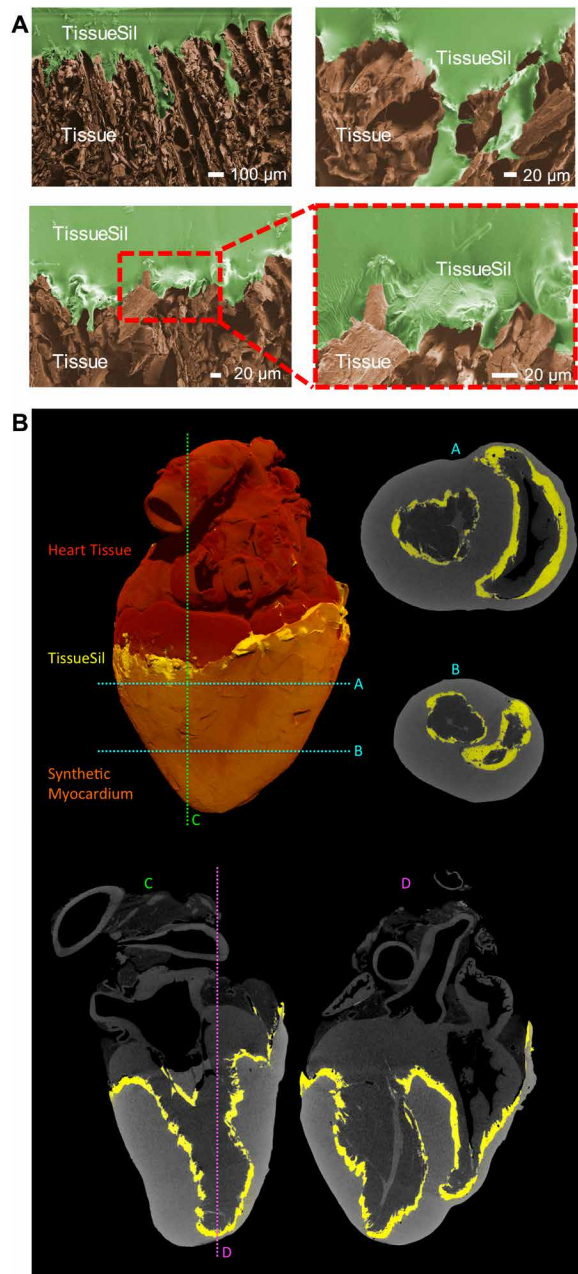


Fig. 3. TissueSil adhesive developed for adhering preserved tissue to a soft robotic matrix. (A) SEM images of the TissueSil (green) and its interface with preserved tissue (brown). (B) MicroCT images of the passive biohybrid heart. The yellow color represents the TissueSil adhesive at the tissue/silicone interface. Color scale (yellow to red) according to high to low electron density.

reduce the number of fabrication steps that were previously described for flat pleated actuators (30, 31). Figure 5A shows the layer-by-layer fabrication process. Briefly, two thin silicone sheets formed the outer layers, and paper pleat layers formed the strain-limiting layers on each side of a water-soluble mask [polyvinyl alcohol (PVA) sheet]. The actuator assembly was bonded using uncured silicone, and the PVA was subsequently dissolved to form a zero-thickness bladder. The actuator geometry was tuned by laser cutting the paper pleat and PVA layers into desired shapes (varying parameters such as chamber

size, number, and arrangement of actuators). This method enabled facile, rapid manufacturing for scaling up the number of actuators in a soft matrix (see the “Fabrication of the soft robotic myocardial band” section in Materials and Methods; fig. S2).

On pressurization, the fPAMs contract axially and expand in the orthogonal direction (henceforth referred to as radially due to the expanded shape). The depressurized and pressurized behavior of the actuators was characterized for various chamber sizes (14- and 20-mm square bladders), as shown in Fig. 5 (B and C). We created a finite element (FE) simulation of the actuators in Abaqus (Dassault Systèmes). The contraction of the actuators increased with higher pressure and agreed with the FE model prediction (Fig. 5B). Although the actuators underperformed compared with numerical prediction, the trend was consistent with FE simulations (Fig. 5C). We measured the isometric force generation that the actuators could generate under cyclical pressurization with a universal materials tester (Instron 5944), using an electropneumatic control box to pressurize and depressurize the actuators, as previously described (29). The FE model predicts an approximately linear correlation between input pressure and peak measured force (Fig. 5D), whereas the experimental results show slightly lower forces than those predicted numerically at higher pressures, likely due to slipping of the test specimens from the grips of the tensile testing machine at increased pressures. On the basis of this characterization, we opted for 20-mm actuators, because both contraction and force generation were greater than those of 14-mm actuators. An aspect ratio of bladder (L/W) of 1 was selected on the basis of a computational parametric study that predicted an optimal value for contraction between 1 and 1.5 for contraction (Fig. 5E).

Characterization of multiple-array matrices of soft robotic cardiac muscles

Next, we characterized contraction and force generation for arrays of fPAMs. We conducted numerical simulations on serial and parallel arrays of actuators. Maximum contraction was similar for all serial (one-by-one, two-by-one, and three-by-one) (Fig. 6A) and parallel (one-by-one, one-by-two, and one-by-three) (Fig. 6B) arrays of 20-mm bladders. Force generation was similar for additional actuator chambers connected in series (Fig. 6A), whereas force increased linearly with the number of actuators in parallel (Fig. 6B). We tested the contraction of a three-by-three array of actuators and compared results with the FE model (Fig. 6C). About 15% contraction was generated at maximum pressure, which was similar to single actuator specimens (three-by-one array) that generated contraction of 16%. FE simulation of a three-by-three array showed very good agreement at lower pressures but underestimated at higher pressures (Fig. 6C). We characterized the effect of actuator spacing computationally (Fig. 6D). The spacing of actuators in an array did not have a substantial effect on contraction percentage. In Fig. 6E, we made an array of circumferential actuators (five-by-one array) that match the diameter of the porcine left midventricle. We measured area reduction upon pressurization, using imaging software. With increasing pressure, area reduction increased, up to 90% at 2.5 psi, demonstrating the capability of the actuator array to reduce left ventricular chamber size upon actuation.

Design and construction of a bioinspired soft robotic myocardial band

Inspired by the left ventricular portion of the HVMB, we constructed a soft robotic myocardium. The unraveling of the heart into the

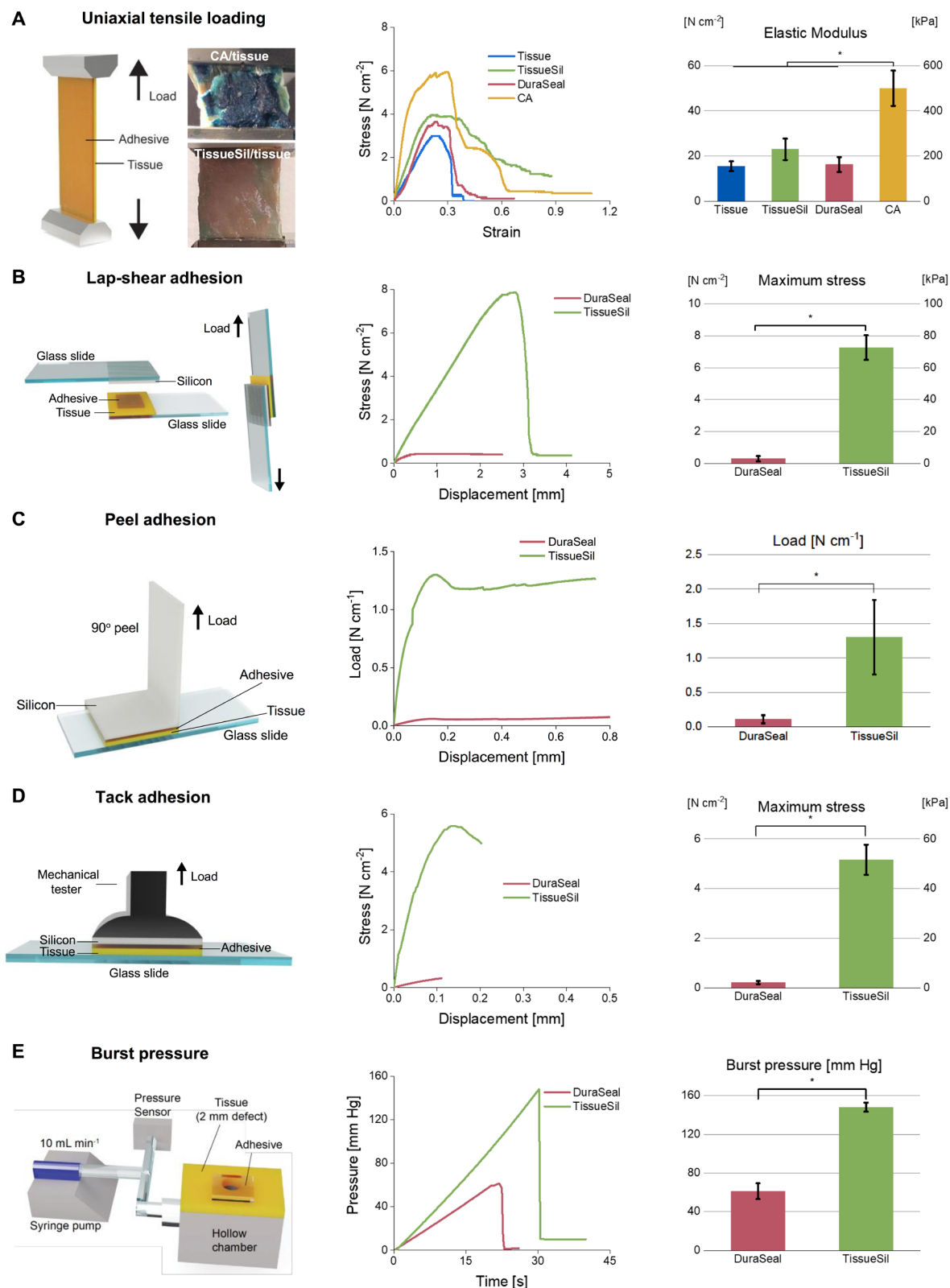


Fig. 4. Mechanical characterization of adhesive/tissue interface and comparison with commercially available tissue adhesives. For (A) to (E), subpanels are as follows: test setup (left), representative data from each group tested (middle), and summary data (right). (A) Uniaxial tensile testing of samples of tissue coated with adhesive. Inset in (A) shows cracking of CA and co-stretching of TissueSil during tensile loading. (B) Lap shear adhesion test. (C) 90° peel test. (D) Tack adhesion testing. (E) Burst pressure testing. Data are means \pm SD ($n = 3$). * $P < 0.05$ using one-way ANOVA with post hoc Tukey test.

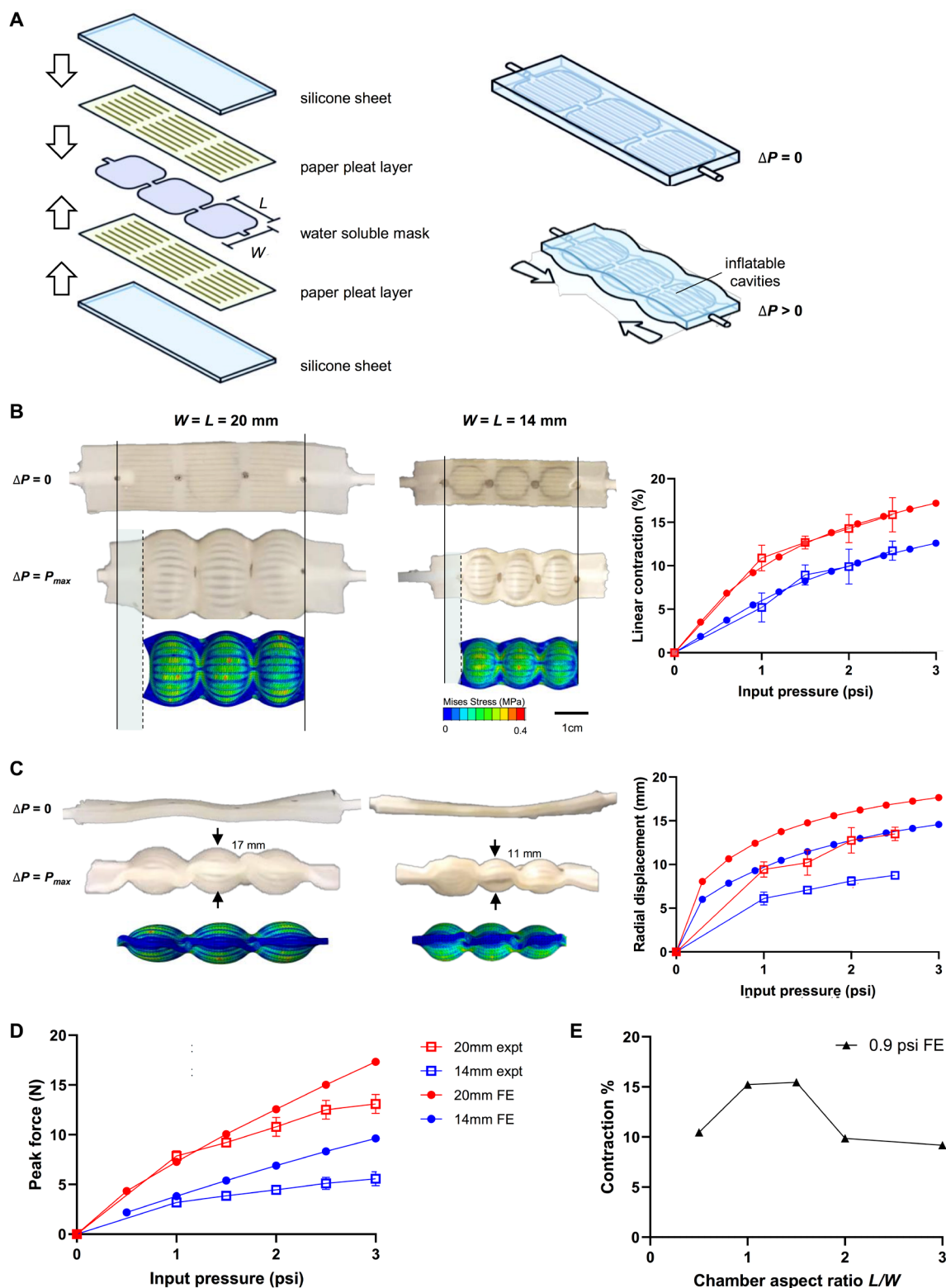


Fig. 5. Fabrication and mechanical and computational characterization of single-array fPAMs. (A) Fabrication process for fPAMs. Comparisons of (B) linear contraction ($n = 5$ for 20 mm by 20 mm and $n = 4$ for 14 mm by 14 mm) and (C) radial displacement ($n = 3$) measured experimentally and predicted computationally at $P = \Delta P_{max}$. (D) Force generation for increasing input pressures measured experimentally ($n = 6$) and predicted computationally. (E) Computational prediction of percentage linear contraction for various aspect ratios (L/W). Data are means \pm SD. L = length of bladder, W = width of bladder, P = actuation input pressure. $\Delta P_{max} = 2.5$ psi.

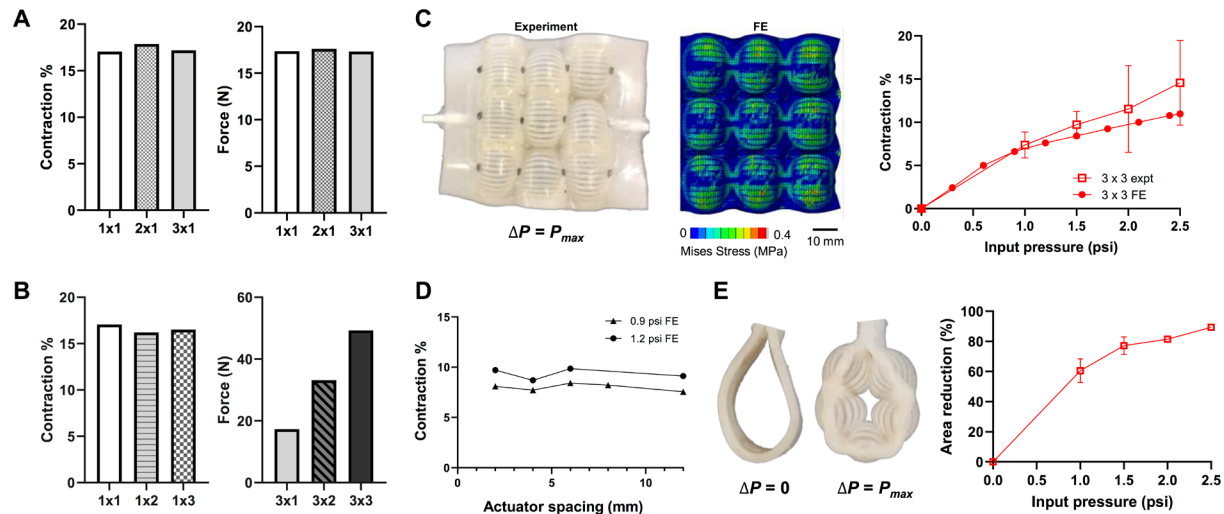


Fig. 6. Characterization of multiple-array matrices of soft robotic cardiac muscles. (A) FE prediction of contraction percentage and force generation of serial arrays (one by one, two by one, and three by one). (B) Modeling of contraction percentage (one-by-one, one-by-two, and one-by-three) and force generation (three-by-one, three-by-two, and three-by-three) of parallel arrays. (C) Contraction of a three-by-three array experimentally (left) and computationally (middle) at ΔP_{\max} . The contour plot shows Mises stresses in the FE simulation. The graph shows percentage contraction at different input pressures (right). (D) FE prediction of contraction for different actuator spacing in an array. (E) Inner area reduction of a circumferentially oriented single array with increasing pressure. Photos (left) are uninflated and inflated states at ΔP_{\max} . $\Delta P_{\max} = 2.5$ psi. Data are means \pm SD. $n = 3$.

ventricular myocardial band is shown in Fig. 7A and movie S2. Figure 7B depicts how we used DT-MRI to identify the directions of greatest diffusion in tissue, corresponding to the cardiomyocyte orientation of the dissected band. This imaging technique enabled replication of the fine myocardial structure with an active synthetic substitute. First, we took the apical loop of the unraveled band (ascending and descending segments) and scanned it with DT-MRI. Using a MATLAB script, we located the sub-epicardial surface and outer contour of the heart. We then projected the DT-MRI data on a 2D plane and performed tractography to visualize the cardiac myofiber directions, as can be seen in Fig. 7B. Next, we generated a coarser grid containing the principal diffusion directions. On the basis of these two datasets, a soft robotic myocardial band was designed with an array of actuators following the fiber orientations of the unraveled band in a computer-aided design package (SolidWorks). We then manufactured the 2D soft robotic myocardial band using the methods described in the previous section.

Assembly, actuation, and imaging of the biorobotic hybrid heart and comparison with in vivo and in silico heart models

We first wrapped the soft robotic myocardial band in a 3D helical fashion around the left ventricular and the interventricular septal endocardial tissue from a dissected, preserved porcine heart with intact intracardiac structures (structure previously shown in Fig. 2B) (Fig. 8A). Next, this tissue/soft robotic band assembly was supported in the outer mold (cast as described in Fig. 2A), and any remaining space between them was cast with Ecoflex 00-20 (see the “Assembly and actuation of the biorobotic hybrid heart” section in Materials and Methods), the same material as the soft robotic myocardial band, resulting in seamless integration with the actuators (Fig. 8B and movie S3). The resulting biorobotic hybrid heart had an actuable myocardial wall, with minimal actuator air cavity in the deflated state (Fig. 8B), and intact endocardial structures that we could image with an endoscopic camera (Fig. 8C).

We actuated the biorobotic hybrid heart while performing 4D MRI to observe whether the soft robotic myocardium and organic endocardium are coupled (Fig. 8D and movie S4). With MRI, we can visualize the movement of the ventricular walls as the fPAMs inflate and deflate and the conformability of the synthetic myocardium to the endocardial tissue throughout the cardiac cycle (movie S4). We observed left ventricular chamber reduction and wall thickening between the end of the filling cycle (end-diastole, where the internal pressure of the fPAMs is zero) and end of the ejection cycle (end systole, where the internal pressure of the fPAMs is positive). The interventricular septum is engaged in this movement and moves as a part of the left ventricle, which is difficult to achieve with existing flow-driven benchtop models.

The contractile motion of the biorobotic hybrid heart was evaluated and compared with an in vivo and in silico healthy heart (the same heart we used to guide HVMB-inspired design shown in Fig. 7). Echocardiography of the healthy porcine heart was acquired (Fig. 8E) before explant. After the heart was explanted, we conducted DT-MRI scanning of the intact heart and used these data to construct a dynamic FE model based on its 3D geometry and fiber orientation (fig. S5). We observed a similar chamber size reduction in the biorobotic hybrid heart compared with its corresponding in vivo and in silico models in both the short- and long-axis views (fig. S6). The ejection fraction from the biorobotic hybrid heart is 68%, showing close agreement with both in vivo and in silico models, which had ejection fractions of 69 and 70%, respectively. These values are within expected physiological ranges (41).

DISCUSSION

In this work, we demonstrate a technological platform for creating an autonomously beating heart. To overcome the current limitations in both synthetic manufacturing and tissue engineering, we present a biohybrid approach to replicating the heart. Existing biohybrid

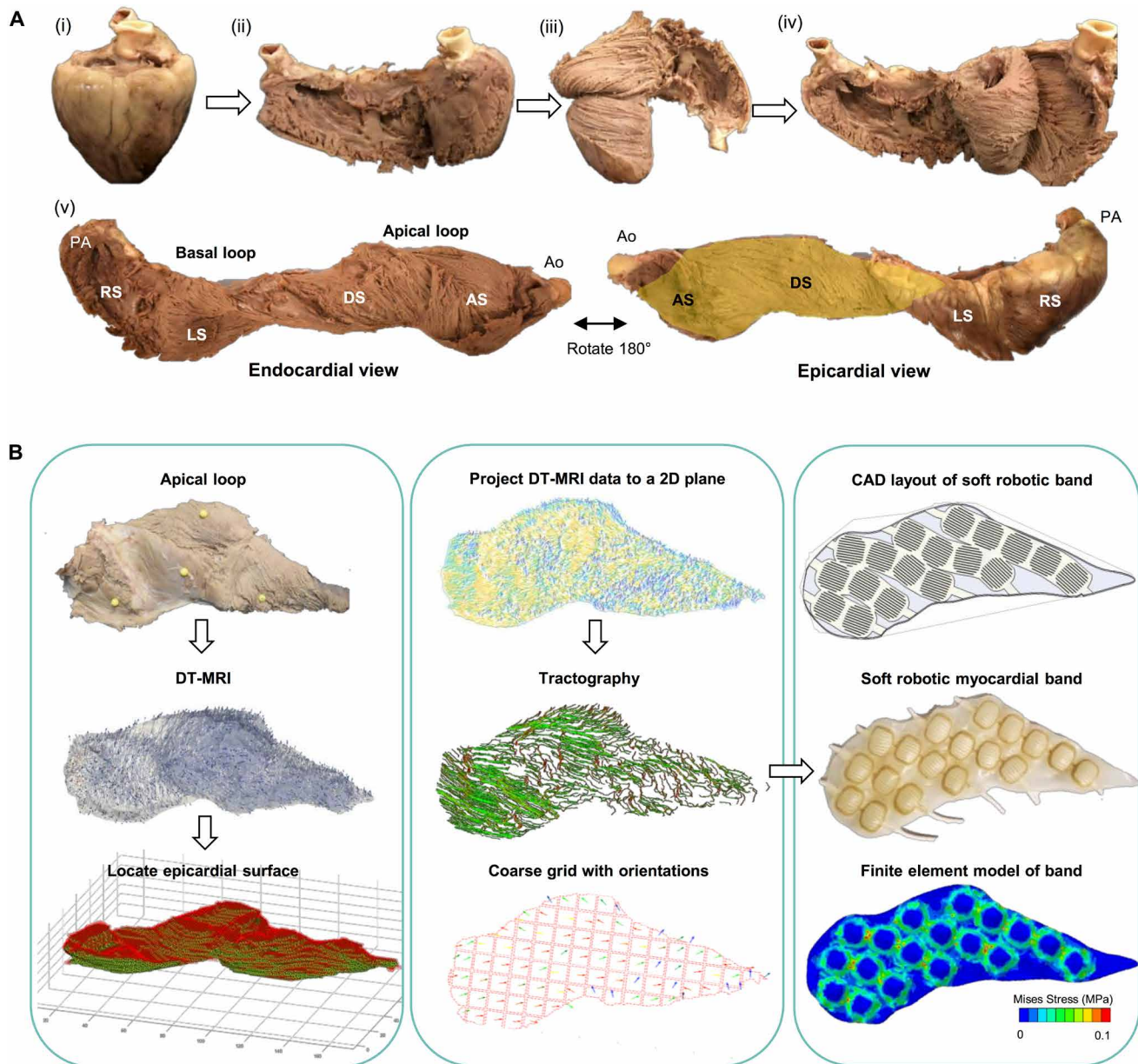


Fig. 7. Inspiration and design process for soft robotic myocardial band. (A) Unraveling of the HVMB. PA, pulmonary artery; Ao, aorta; RS, right segment; LS, left segment; DS, descending segment; AS, ascending segment. (B) An illustration of the bioinspired process of fabricating the synthetic band. (Left) Isolation of the left ventricular band, DT-MRI image data, and process of locating the epicardial surface. (Central) Projection of DT-MRI data at epicardial surface onto a 2D plane, tractography data, and a coarser grid with principal orientations. (Right) Computer-aided design model of bioinspired band, the physical soft robotic myocardial band, and the Mises stress contour plot from the FE model of the actuated band at ΔP_{\max} .

robots use living cells or tissues as actuators and synthetic materials as passive structures (42–44) but have limited scalability. To recreate the heart at the organ scale, we exploited rapidly developing techniques in soft robotics (8, 9, 14, 29) to emulate complex biological motions and used organic tissue structures for accurate anatomical representation. Our resulting biorobotic hybrid heart has accurate anatomical details (including valves, papillary muscles, moderator bands, chordae tendineae, vessels, and ventricular walls) while exhibiting complex 3D cardiac motion. With this model, we demonstrate

a physiological level of contractile motion. We also demonstrate engagement of the interventricular septum, which presents an improvement over current passive models that are driven by internal or external pressure or flow.

Compared with ex vivo beating heart or in vivo animal hearts, our platform offers additional advantages with user flexibility and tunability. Because we used fixed tissues, all components in our heart model have longevity, allowing users to operate the heart on demand and perform repeated testing. In addition, owing to the use

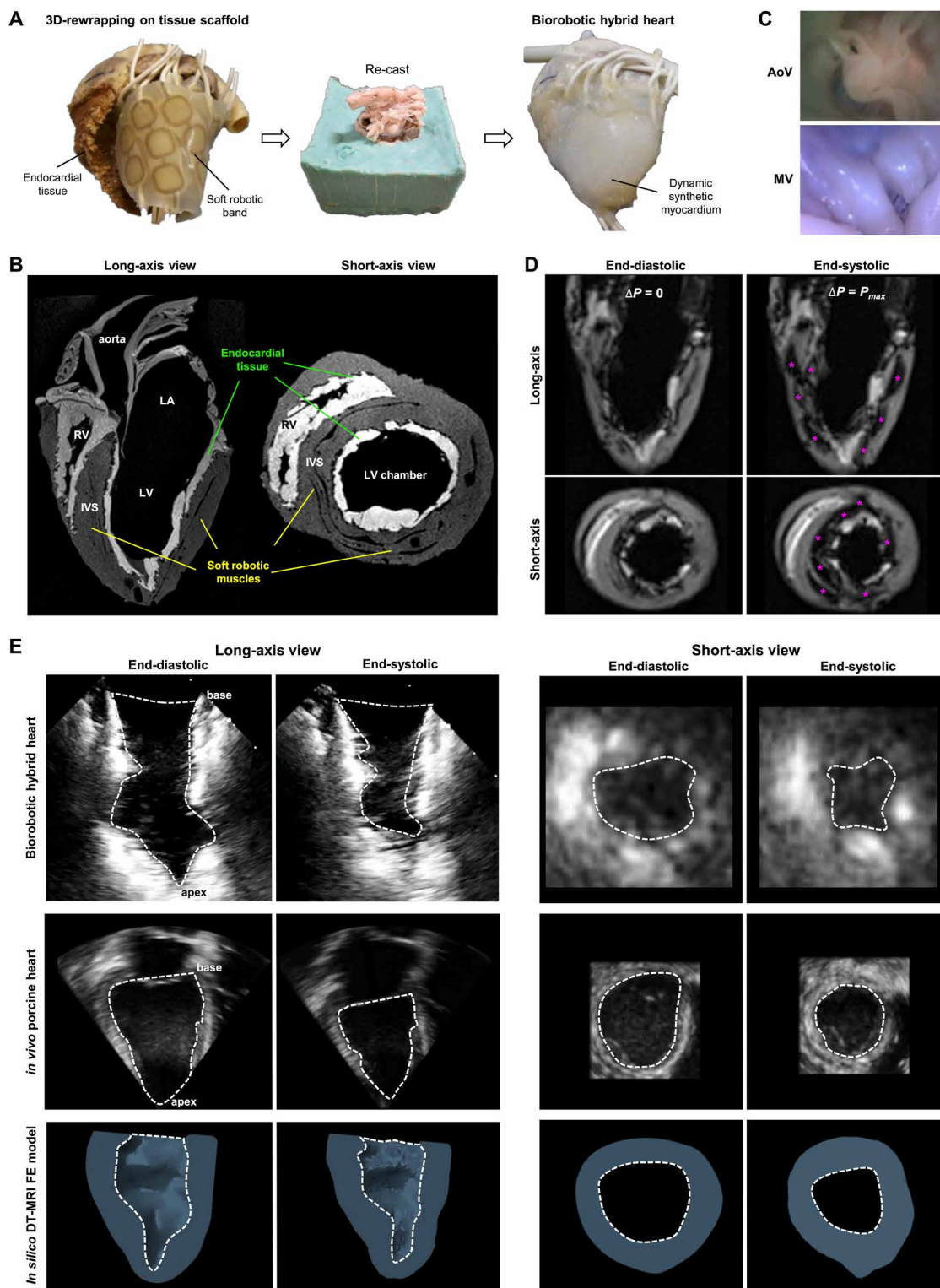


Fig. 8. Assembly and actuation of the biorobotic hybrid heart and comparison with the *in vivo* and *in silico* native heart models. (A) Assembly and construction of the biorobotic hybrid heart. (B) Structural images of the biorobotic hybrid heart from MRI imaging in the long-axis and short-axis views. LV, left ventricle; LA, left atrium; RV, right ventricle; IVS, intraventricular septum. (C) Endoscopic images of the intact aortic (top) and mitral valves (bottom). (D) End-diastolic and end-systole GRE CINE images in the long- and short-axis views. Purple asterisks show actuator cavity, which expands at end systole ($\Delta P = P_{max}$). (E) Contractile motion of the biorobotic hybrid heart in comparison with other heart models. (Top) Biorobotic hybrid heart actuation recorded by echocardiography. (Middle) *In vivo* porcine heart imaged by echocardiography. (Bottom) FE prediction of DT-MRI-based left ventricle model at physiological contractility. White dashed line shows left ventricular chamber.

of synthetic, tunable components, we could precisely control the motion of the heart. Cardiac parameters—such as heart rate, contractility, and stroke volume—can be tuned via an electropneumatic control system [described in previous studies (29)] that controls individual actuators. This allows simulation of extreme conditions, like exercise, or diseased conditions that may better represent the target patient population for intracardiac devices, such as heart failure (weaker actuation) or myocardial infarction (locally inactivated muscles). Furthermore, the soft robotic myocardium component may also be programmed to mimic a “patient-specific” cardiac fiber orientation and its resulting motion via *in vivo* DT-MRI (45, 46).

In the development of the biorobotic hybrid heart, several technological hurdles had to be overcome. First, we needed a reliable adhesive interface between the synthetic and organic components in a wet, dynamic environment. Because there were no commercially available adhesives for this application, we developed a silicone-based soft adhesive, which we call TissueSil, which has high adhesion strength, ability to tolerate physiological deformations without changing tissue mechanical properties, and function in wet environments. Our adhesive allows conformable, flexible coupling of the tissue-silicone interface, which may be useful for future avenues in macroscale biohybrid robotics. Next, inspired by the HVMB theory, we used a simplified 2D design and fabrication strategies to make a functional 3D assembly, replicating the complex 3D fiber architecture of cardiac muscles. In this process, we demonstrated use of DT-MRI to translate actual fiber architecture of cardiac tissues into an actuable biomimetic matrix. This led to the development of a programmable, flat soft robotic matrix whose individual linear actuators could be oriented to match the cardiac tissue fibers and subsequently reconfigured into a 3D helix to represent the 3D fiber architecture as well as the global cardiac motion.

There are several limitations of this study, which we will endeavor to overcome with future iterations of the model. For a proof-of-concept study, we focused on replicating the most important function of the heart—that is, the contractile motion that displaces blood from the left ventricle. Therefore, we only actuated the left ventricle. Although we replicated the overall displacement of fluid, the displacement was aided by the radial expansion of individual actuators surrounding the endocardial tissue. fPAMs generate lower contraction and higher radial expansion compared with native cardiomyocytes, resulting in an exaggerated myocardial wall thickening during the systolic phase. Improvements in contractility with lower degrees of radial shortening are desirable for enhanced physiological motion, such as myocardial shortening and thickening. In this work, we used the HVMB theory (22–25) as an inspiration, to map fibers from 3D to 2D, for subsequent rewinding around the tissue structures. We acknowledge that there is some controversy surrounding HVMB theory (47, 48) and that the continuous myocardial mesh model is more compatible with recent scientific research (49), but for the purpose of this work, it provided a reasonable basis for guiding simplified biomimetic soft actuators. Last, we did not recapitulate the hemodynamics of the blood inside the heart. In the future, we will connect this heart to an instrumented mock circulatory loop to recreate the hemodynamics, specifically the pressure-volume loops of the heart for each cardiac cycle.

The biorobotic hybrid heart has potential utility as a high-fidelity simulator for interventional cardiology applications, specifically involving minimally invasive procedures (such as self- or balloon-expanding valve prostheses or occluder devices). The overall vision of this work is to be able to recreate accurate patient-specific hemo-

dynamics. DT-MRI is currently being performed on human patients *in vivo*, and we could conceivably image a patient, create a patient-specific soft robotic model, test an intracardiac device in a mock circulatory loop with the biorobotic hybrid heart (for example, a prosthetic valve), and thus optimize its application to the patient (for example, for reducing paravalvular leakage). With a longer shelf life and user controllability, this platform heart model may allow faster evaluation and design iterations of intracardiac devices compared with *in vivo* testing. The model also has potential utility for device demonstration, because it is compatible with various clinical imaging modalities, such as MRI, echocardiography, and computed tomography. Medical device companies often offer training of their devices to interventional cardiologists, in which a portable, anthropomorphic, functional heart model, as presented here, would be beneficial. Overall, a robust model that can faithfully represent cardiac motion and preserve intracardiac organic structures may be a valid alternative or supplement to animal testing for intracardiac device testing and demonstration.

MATERIALS AND METHODS

Ex vivo heart casting of the outer mold

A freshly explanted porcine heart was obtained within 4 hours of sacrifice and thoroughly washed to remove excess blood and blood clots. Then, it was soaked in phosphate-buffered saline at a 1 M concentration (VWR) at 4°C for 30 min and washed to clear any remaining blood from the inside of the heart. Next, it was submerged in 10% formalin (Carolina Biological Supply) at room temperature for 3 days and subsequently rinsed with 1 M phosphate-buffered saline twice and stored in 4°C. An outer mold for the ventricular wall was cast before the dissection of the myocardial tissues. First, the fixed heart was positioned upside down, with the atria and vessels anchored in sulfur-free clay (Smooth-On) in a custom-made acrylic box, leaving only the ventricular walls exposed. Next, silicone (Mold Star 15, Smooth-On) was poured into the assembly until the entire ventricle was covered and then left to cure at room temperature for at least 5 hours. Subsequently, the box was disassembled, and the outer mold was obtained by detaching and removing the heart and clay. This casting serves as the outer mold for the final casting step of the biohybrid heart. Approval for working with *ex vivo* animal tissue has been obtained from the Committee on Animal Care at the Massachusetts Institute of Technology (protocol number 0118-006-21).

Ex vivo heart dissection

The epicardial and myocardial tissue was removed by hand dissection. The outermost layer was removed after the myocardial fiber orientation. Next, starting at the right side of the anterior interventricular sulcus, which separates the right and left ventricle, the left ventricular free wall tissue was removed along the fiber orientation in a layer-by-layer manner until the transmurally changing fiber orientation became circumferential (or 0° to the base plane) (Fig. 2B). This circumferential fiber direction indicated a continuum of the left ventricle in the interventricular septum and was used as a guide to separate the right ventricle from the left ventricle. The myocardial tissue of the left ventricle was trimmed until the fiber orientation became helical (60°), which indicates that transmural depth has reached the endocardial layer. The right ventricular part of the interventricular septum was also further trimmed. This dissection process results in a heart with the endocardial layer and the intracardiac structures intact but without the myocardial tissues. Defects

in the tissue created by the dissection process were repaired with a small amount of 2-octyl CA-based adhesive (KEG-500, Starbond) before the final molding step.

Casting of an elastomeric myocardial shell

Ecoflex 00-20 (Smooth-On) was mixed at a 1:1 ratio (as indicated by the manufacturer) using a planetary centrifugal mixer (ARE-310, Thinky) for 30 s at 2000 rpm, followed by a degassing step for 30 s at 2200 rpm. Next, the mixture was placed in a vacuum chamber until air bubbles disappeared. The silicone was then poured into the outer mold, fabricated as described above. Next, endocardial heart tissue with the outer layers removed, as described above, was blotted dry with a Kimwipe on the outer cut surface. The tissue was carefully placed in the outer mold in the uncured silicone. The atria and great vessels were covered with food wrap to prevent drying, and the assembly was cured at room temperature for 4 hours. The tissue was then removed from the elastomeric shell for subsequent adhesion at the tissue/elastomer interface.

Adhesion of fixed tissue and elastomer

PDMS (Sylgard 184, Dow Corning) was prepared by mixing the base and curing agents in a ratio of 20:1 using a planetary centrifugal mixer (ARE-310, Thinky) at 2000 rpm for 30 s, followed by degassing at 2200 rpm for 30 s. Then, 1% (v/v) triethoxyvinylsilane (Sigma) and 1% (v/v) 3-(triethoxysilyl)propyl isocyanate (Sigma) were added and mixed in the same way. Last, 0.8% (v/v) platinum catalyst (Sigma) was added and mixed in the final step to adjust the curing time needed to coat the surface. Forty grams of this mixture was prepared for coating the surface of the endocardial tissue. The adhesive solution was applied onto the tissue surface using a high-density sponge along the fibers to minimize the formation of air bubbles. After assembling the tissue with premade silicone myocardium, it was left at room temperature for 20 min to cure and then stored in 4°C overnight without mechanical disruption to allow coupling chemistry to occur before using the heart.

Morphology of cross-sectioned TissueSil/tissue interface

TissueSil/fixed myocardial tissue substrates were sectioned perpendicular to the adhesive plane and freeze-dried for 12 hours. SEM images were obtained by Zeiss Merlin high-resolution SEM at an acceleration voltage of 1 kV and a working distance of 5 to 6 mm.

Adhesion characterization of TissueSil

Uniaxial tensile test

Laminates were evaluated with an Instron 5944 mechanical tester. Fixed tissue substrates of 3 cm by 2 cm and 2-mm thickness were cut using a ceramic knife. Next, a 0.5-mm-thick layer of TissueSil, DuraSeal, or CA adhesive was spread evenly over the tissues. Once cured, the adhesive/tissue composites were loaded using mechanical vice style grips onto the mechanical fixture and uniaxially stretched at a rate of 10 mm min⁻¹. TissueSil was mixed with Silc Pig (Smooth-On), and CA and DuraSeal were mixed with dye (Indigotine and Fast Green FCF) for better visual representation.

Lap shear strength

Maximum lap shear at failure was measured according to a modified American Society for Testing and Materials (ASTM) F2255-05 protocol. Fixed myocardial tissue sections (2 cm by 2 cm) and silicone (Ecoflex) sheets were adhered on microscopic glass slides using Loctite 422 and Sil-Poxy (Smooth-On) adhesives, respectively.

A 0.3-mm-thick layer of adhesive was sandwiched between the silicone sheet and myocardium tissue. TissueSil, DuraSeal, and CA adhesives were cured for 12 hours and 2 and 5 min, respectively. Lap shear strength was quantified using a mechanical tensile tester fixed with a 2-kN load cell (Instron 5944), with a linear extension of 3 mm min⁻¹.

Peel strength

Peel strength was quantified according to a modified ASTM D6862-11 protocol. Fixed myocardial tissue sections (2 cm by 2 cm) were adhered on microscopic glass slides using Loctite 422 CA adhesive. A silicone sheet (7 cm by 2.5 cm) was adhered on the myocardium tissue substrates using TissueSil, DuraSeal, and CA adhesives. A 90° peel test was conducted using a 5944 Instron mechanical tensile tester, and maximum force at delamination was recorded by elongating at a rate of 3 mm min⁻¹.

Tack adhesion

Fixed myocardium tissue sections (2 cm by 2 cm) and silicone (Ecoflex) sheets were adhered on microscopic glass slides using Loctite 422 and Sil-Poxy adhesives, respectively. A thin layer (0.3 mm) of the adhesive was applied between the myocardium tissue and silicone sections. The pull-off strength was measured using a 5944 Instron mechanical tester at an elongation rate of 3 mm min⁻¹. Silicone sheet detachment from the tissue surface was quantified as the maximum load before failure.

Burst pressure

The hydraulic burst pressure was performed according to a modified ASTM F2392-04 protocol. Fixed porcine myocardium tissues were cut to a dimension of 2 cm by 2 cm, and a 2-mm defect was created at the center using a 13-gauge needle. A syringe pump was connected to the pressure sensor and a 1.5-ml hollow chamber using a T-connector. The upper piece of the hollow chamber had a 10-mm-diameter opening, and tissue substrates were placed over it and secured using a flange. A 0.3-mm layer of adhesive was spread over the defect. Air (10 ml min⁻¹) was inserted into the cavity, and burst pressure was recorded via the pressure sensor (TruWave, Edwards Lifesciences).

MicroCT imaging of the adhesive conformability

We visualized the conformation of TissueSil (10% barium sulfate as a contrast agent) to the fixed heart tissue and synthetic myocardium by means of microCT with an X-Tek XRA-002 microCT system (Nikon Metrology Inc., Brighton, MI). The 3D reconstructions were performed using CT-Pro (Nikon Metrology Inc., Brighton, MI), and surface renderings were generated using VGStudio Max (Volume Graphics GmbH, Heidelberg, Germany).

Characterization of actuators

For linear contraction and radial displacement characterization, the actuator specimens were dynamically actuated for 300 ms at 60 beats per minute (bpm) using a custom electropneumatic control system. All specimens were marked with optical trackers, and the motion was video-recorded at 60 frames per second. Screenshot images of the specimens were analyzed by tracking the relative displacements of optical markers and quantified using a MATLAB script. Dynamic force was measured for actuator specimens using a mechanical tester (Instron 5944). The specimens were held at a fixed position and dynamically actuated for 300 ms at 60 bpm to record the force. The peak force was calculated and averaged over 10 peaks for analysis. For area reduction characterization, circumferential actuator specimens were dynamically actuated and video-recorded

as before. The screenshots were processed using an image processing tool (ImageJ) to calculate the change in the inner area of the actuators.

FE modeling of the actuators

Abaqus/Standard 2017 (Dassault Systèmes, Vélizy-Villacoublay, France) was used to calculate the quasi-static solution of the FE model to predict linear contraction, radial expansion, and force generation as well as to optimize the actuator design. Ecoflex 00-20 was modeled as hyperelastic and isotropic material using a three-term Ogden strain energy potential material model [$\mu_1 = 0.005954916846 \text{ N mm}^{-2}$; $\mu_2 = 0.002746417247 \text{ N mm}^{-2}$; $\mu_3 = 0.00905891419 \text{ N mm}^{-2}$; $\alpha_1 = 3.98529341$; $\alpha_2 = 2.47960094$; $\alpha_3 = -3.58683068$; $D_1 = D_2 = D_3 = 0 \text{ (N mm}^{-2})^{-1}$] and 10-node quadratic tetrahedron solid elements with a hybrid formulation (C3D10H). The hyperelastic properties were determined with an Instron 5944 universal testing system using the uniaxial tensile testing procedure according to the ASTM 412 standard (specimen design: type C; number of samples: $n = 5$). For the paper material, 3D linear quad-dominated shell elements (S4R) with reduced integration were used to model the very thin paper pleats. In a uniaxial tensile test (ASTM D828; number of samples: $n = 8$), linear elastic material behavior of the 45% polyester/55% cellulose blend paper was derived for small strains (<3%) corresponding to the strains identified in the simulated shell elements. A Young's modulus of 120 MPa was derived from the slope along the experimentally found nominal stress/strain curve. For the incompressible material, a Poisson's ratio of 0.499 was chosen.

The accuracy of the mesh was ascertained through a mesh refinement study, resulting in mesh seedings of 0.9 mm for the silicone matrix and 0.6 mm for the shell elements of the strain-limiting layer. To avoid extensive distortion of elements along the very thin air cavities (300 μm), we refined the mesh to a seeding size of 0.4 mm in those areas. The interaction between the two material structures was simplified by fixing the shell elements of the paper (slave) to the outer surface of the silicone (master) using tie constraints. As boundary conditions, elements on one of the end faces of the actuator were fixed in all six degrees of freedom to measure the maximal linear and radial displacement. To derive the generated force of an actuator, these boundary conditions were applied to nodes on both ends. A uniformly distributed linear pressure with a magnitude of 3 psi was applied to the surfaces of the air cavities over an equally spaced time frame of 1 s with an initial time increment of 0.01 s.

Helical ventricular myocardial band

A freshly explanted porcine heart was dissected following Torrent-Guasp's simple hand dissection method. The heart was first boiled in water for about 20 min to soften the tissue. The vessels and atria were removed so that only the ventricular myocardial tissue remained (Fig. 7A, i). First, the right ventricular tissue was separated by dissection starting from the left side of the anterior interventricular sulcus, detaching the pulmonary artery from the aorta (Fig. 7A, ii). At the posterior limit of the right ventricular cavity, where the free right ventricular wall meets the septum, the cleavage plane was dissected all the way to the aorta (Fig. 7A, iii). The descending fibers were separated from the superficial layers. Next, the cleavage plane was identified in the septum by the sudden change in the fiber orientations from horizontal to vertical directions. The layers were separated along the natural fiber directions (Fig. 7A, iv). The aorta was separated from the rest of the heart by cutting the right fibrous trigone. The

entire structure was unraveled into a single ventricular myocardial band (Fig. 7A, v) (see movie S1).

Fabrication of the soft robotic cardiac muscles

Sheets of Ecoflex 00-20 of 1.2-mm thickness were prefabricated in house by depositing prepolymer solution using a silicone applicator, followed by curing at room temperature for about 1.5 hours. The paper pleat layer was made using wiper papers (polyester/cellulose blend paper, VWR), and the air chambers was formed using a water-soluble PVA mask (Ultra Solvy stabilizer, Sulky). Both paper pleats and water-soluble mask were laser-cut into defined geometries. Before assembly procedure, the paper layer was wet with about 40 g of uncured Ecoflex 00-20 prepolymer liquid and degassed to ensure proper integration of paper and elastomer (fig. S2B). Then, PVA was sandwiched between two paper pleat sheets for the inner layers and two silicone sheets on the outer layers and bonded using uncured Ecoflex 00-20 (fig. S2, C and D). A flat plate was used to apply even pressure on top of the assembly to form a good seal. The assembly was cured in the oven at 60°C for 20 min or room temperature about an hour. Once cured, the actuator was trimmed using scissors and injected with water to dissolve the PVA layer and left at room temperature for about an hour (fig. S2E). PVA gel was ejected by rolling a rod on the actuator body. This process was repeated two times. Air supply tubings (1/8" outside diameter silicone tubing, McMaster) were inserted to the ports by preinserting a 1/16" metal rod and then sliding a silicone tubing over, and Sil-Poxy was used to seal the two materials (fig. S2F).

Assembly and actuation of the biorobotic hybrid heart

The biorobotic hybrid heart was assembled by wrapping flat soft robotic bands around the left ventricular endocardial tissue (structure described in Fig. 2B) and casting silicone matrix following the outer ventricular wall geometry using an outer wall mold. The DT-MRI-inspired synthetic band (Fig. 7B), which was fabricated as described in the previous section, was bonded to the endocardial tissue surface starting with the descending segment ends at the posterior side of the left ventricle and ending with the ascending segments placed in the septal space to mimic the left ventricular helicoid. The endocardial tissue was precoated with TissueSil as described in the earlier section and left overnight to complete the reaction chemistry. A prepolymer solution of Ecoflex 00-20 (Smooth-On) was used as an adhesive to bond between the bands and to the tissue surface, and 0.1% platinum catalyst (Sigma) was added to the uncured Ecoflex solution to accelerate the bonding process to about 5 min at room temperature. Before casting the outer wall, pliable metal wires were inserted through the air supply tubings to prevent blockage of the airway during the molding process and pulled out after casting. Ecoflex 00-20 was poured between the tissue band assembly and outer wall and was placed in a vacuum chamber while curing to remove air bubbles in the final construct. After curing at room temperature for 2 hours, the outer mold was demolded. The biorobotic hybrid heart was actuated using an electropneumatic control system, as previously described, and for 400 ms at 40 bpm was used for the MRI motion study.

MRI of biorobotic hybrid heart

Retrospective steady-state gradient recall echo (GRE) cinematographic (CINE) MRI [repetition time (TR) = 5.1, echo time (TE) = 1.4, flip angle = 12°, 1 mm by 1 mm by 6 mm, 24 frames per heartbeat] was performed on a 3T clinical scanner (Connectome, Siemens Healthineers,

Erlangen, Germany) and synced to the 40 bpm pneumatic actuator pumps. CINE GRE MRI was performed over five actuator cycles to reconstruct a high-resolution 2D section and repeated to cover the entire heart. 3D high-resolution structural GRE MRI (TR = 5.1, TE = 1.4, flip angle = 12°, 1 mm isotropic resolution) was performed to identify actuators, silicone myocardium, and ventricular chamber.

Echocardiography

2D and 3D echocardiography of an in vivo porcine heart and the biorobotic hybrid heart was performed by a cardiologist using an iE33 ultrasound machine (Philips) with an X7-2 transducer probe (Philips). For quantitative analysis, a long-axis view was used to make a comparison, because the short-axis view can be inaccurate due to irregular inner chamber geometry. Area reduction was determined from the end-diastolic and end-systolic images of 2D echocardiography. Ejection fraction was determined from the same images using a single-plane long-axis area length method (50). Systolic and diastolic left ventricular chamber area and length was determined in an image processing software (ImageJ) based on manual segmentation of the left ventricle chamber. Short-axis images/movies were obtained from 3D echocardiography using QLAB software (Philips).

Imaging and postprocessing of fiber orientation and FE modeling of the left ventricle

The fiber orientation of both the 2D myocardial band and the 3D intact heart tissues were imaged with DT-MRI (3D multishot spin echo planar imaging, TR = 2500 ms, TE = 45 ms, 1-mm isotropic spatial resolution, five shots, b value = 0, 500 s mm⁻², and 12 directions) using a Siemens Connectome 3T scanner (Siemens Healthineers, Erlangen, Germany). For the 2D myocardial band, the left ventricular portion of the band was isolated. The vector field that indicates the fiber structure was created by obtaining the primary eigenvector of the three-by-three diffusion gradient matrix in each voxel. The data points for the sub-epicardial surface were extracted, and all associated vectors and the surface contour were projected onto a 2D plane. This provided the contour shape of the soft robotic band. Fiber tractography [Fig. 7B based on the fiber alignment continuous tracking “FACT” method (51)] was conducted to interpret the dense vector field into several continuous fiber tracts. The original vector field was also simplified by partitioning the entire band using a 10 mm-by-10 mm grid and assigning the corresponding region-averaged vector to each square in the grid. The fiber tractography and the coarse vector field were used to guide the design of the actuator patterns. All post-processing was conducted using MATLAB (MathWorks Inc., Natick, MA, USA). A similar method was used to process DT-MRI data of the 3D intact heart. Following the methodology described previously (52), the MRI geometry and the DT-MRI fiber structure were converted into Abaqus, creating a subject-specific FE model of the left ventricle.

Statistical analysis

All data are presented as means ± SD ($n = 3$ for adhesion testing). Significance ($P < 0.05$) was assessed by a t test for comparisons between two groups and with a one-way analysis of variance (ANOVA) with Tukey post hoc correction for comparison between more than two groups. OriginPro 2019 64-bit software was used for statistical analysis.

SUPPLEMENTARY MATERIALS

robotics.sciencemag.org/cgi/content/full/5/38/eaay9106/DC1

Fig. S1. TissueSil bonding chemistry and penetration to microstructures.

Fig. S2. Fabrication steps for the flat soft robotic matrix.

Fig. S3. Uniaxial tensile testing of fresh versus synthetic myocardium.

Fig. S4. Cyclic fatigue testing on fixed tissue-adhesive composite.

Fig. S5. Construction of DT-MRI-based FE model of the left ventricle.

Fig. S6. A comparison of cardiac parameters of the biorobotic hybrid heart model with in vivo and in silico heart models.

Movie S1. Tissue-adhesive failure during uniaxial tensile testing.

Movie S2. Dissection of HVMB.

Movie S3. The structure of the biorobotic hybrid heart under MRI.

Movie S4. Visualization of the biorobotic hybrid heart actuation under GRE CINE MRI.

Movie S5. Motion of the biorobotic hybrid heart and its reference in vivo porcine heart under echocardiography.

REFERENCES AND NOTES

1. A. M. Leopaldi, R. Vismara, M. Lemma, L. Valerio, M. Cervo, A. Mangini, M. Contino, A. Redaelli, C. Antona, G. B. Fiore, In vitro hemodynamics and valve imaging in passive beating hearts. *J. Biomech.* **45**, 1133–1139 (2012).
2. R. Vismara, A. M. Leopaldi, M. Piola, C. Asselta, M. Lemma, C. Antona, A. Redaelli, F. van de Vosse, M. Rutten, G. B. Fiore, In vitro assessment of mitral valve function in cyclically pressurized porcine hearts. *Med. Eng. Phys.* **38**, 346–353 (2016).
3. A. M. Leopaldi, R. Vismara, S. van Tuijl, A. Redaelli, F. N. van de Vosse, G. B. Fiore, M. C. M. Rutten, A novel passive left heart platform for device testing and research. *Med. Eng. Phys.* **37**, 361–366 (2015).
4. G. Gelpi, C. Romagnoni, R. Vismara, A. M. Leopaldi, A. Mangini, M. Contino, C. Antona, Intracardiac endoscopic and angiographic view of step-by-step transcatheter aortic valve implantation in a beating porcine heart: Transcatheter valve platform. *Interact. Cardiovasc. Thorac. Surg.* **17**, S148 (2013).
5. E. Chinchoy, C. L. Soule, A. J. Houlton, W. J. Gallagher, M. A. Hjelte, T. G. Laske, J. Morissette, P. A. Iazzo, Isolated four-chamber working swine heart model. *Ann. Thorac. Surg.* **70**, 1607–1614 (2000).
6. Y. Araki, A. Usui, O. Kawaguchi, S. Saito, M. H. Song, T. Akita, Y. Ueda, Pressure-volume relationship in isolated working heart with crystalloid perfusate in swine and imaging the valve motion. *Eur. J. Cardiothorac. Surg.* **28**, 435–442 (2005).
7. A. J. Hill, T. G. Laske, J. A. Coles Jr., D. C. Sigg, N. D. Skadsberg, S. A. Vincent, C. L. Soule, W. J. Gallagher, P. A. Iazzo, In vitro studies of human hearts. *Ann. Thorac. Surg.* **79**, 168–177 (2005).
8. E. T. Roche, R. Wohlfarth, J. T. B. Overvelde, N. V. Vasilyev, F. A. Pigula, D. J. Mooney, K. Bertoldi, C. J. Walsh, A bioinspired soft actuated material. *Adv. Mater.* **26**, 1200–1206 (2014).
9. E. T. Roche, M. A. Horvath, A. Alazmani, K. C. Galloway, N. V. Vasilyev, D. J. Mooney, F. A. Pigula, C. J. Walsh, Design and fabrication of a soft robotic direct cardiac compression device, in *ASME 2015 International Design Engineering Technical Conferences and Computers and Information in Engineering Conference* (ASME, 2015).
10. A. D. Marchese, C. D. Onal, D. Rus, Autonomous soft robotic fish capable of escape maneuvers using fluidic elastomer actuators. *Soft Robot.* **1**, 75–87 (2014).
11. R. V. Martinez, J. L. Branch, C. R. Fish, L. Jin, R. F. Shepherd, R. M. D. Nunes, Z. Suo, G. M. Whitesides, Robotic tentacles with three-dimensional mobility based on flexible elastomers. *Adv. Mater.* **25**, 205–212 (2013).
12. D. Rus, M. T. Tolley, Design, fabrication and control of soft robots. *Nature* **521**, 467–475 (2015).
13. F. Daerden, D. Lefeber, Pneumatic artificial muscles: Actuators for robotics and automation. *Eur. J. Mech. Environ. Eng.* **47**, 10–21 (2000).
14. S. C. Obajulu, E. T. Roche, F. A. Pigula, C. J. Walsh, Soft pneumatic artificial muscles with low threshold pressures for a cardiac compression device, in *ASME 2013 International Design Engineering Technical Conferences and Computers and Information in Engineering Conference* (ASME, 2013).
15. R. L. Truby, J. A. Lewis, Printing soft matter in three dimensions. *Nature* **540**, 371–378 (2016).
16. T. J. Wallin, J. Pikul, R. F. Shepherd, 3D printing of soft robotic systems. *Nat. Rev. Mater.* **3**, 84–100 (2018).
17. L. A. Macqueen, S. P. Sheehy, C. O. Chantre, J. F. Zimmerman, F. S. Pasqualini, X. Liu, J. A. Goss, P. H. Campbell, G. M. Gonzalez, S. J. Park, A. K. Capulli, J. P. Ferrier, T. Fettah Kosar, L. Mahadevan, W. T. Pu, K. K. Parker, A tissue-engineered scale model of the heart ventricle. *Nat. Biomed. Eng.* **2**, 930–941 (2018).
18. Y. S. Zhang, K. Yue, J. Aleman, K. Mollazadeh-Moghaddam, S. M. Bakht, J. Yang, W. Jia, V. Dell’Erbia, P. Assawes, S. R. Shin, M. R. Dokmeci, R. Oklu, A. Khademhosseini, 3D bioprinting for tissue and organ fabrication. *Ann. Biomed. Eng.* **45**, 148–163 (2017).
19. T. J. Hinton, Q. Jallerat, R. N. Palchesko, J. H. Park, M. S. Grodzicki, H. J. Shue, M. H. Ramadan, A. R. Hudson, A. W. Feinberg, Three-dimensional printing of complex biological structures by freeform reversible embedding of suspended hydrogels. *Sci. Adv.* **1**, e1500758 (2015).
20. P. T. Moser, H. C. Ott, Recellularization of organs: What is the future for solid organ transplantation? *Curr. Opin. Organ Transplant.* **19**, 603–609 (2014).

21. M. S. Lundberg, J. T. Baldwin, D. B. Buxton, Building a bioartificial heart: Obstacles and opportunities. *J. Thorac. Cardiovasc. Surg.* **153**, 748–750 (2017).
22. F. Torrent-Guasp, G. D. Buckberg, C. Clemente, J. L. Cox, H. C. Coghlan, M. Gharib, The structure and function of the helical heart and its buttress wrapping. I. The normal macroscopic structure of the heart. *Semin. Thorac. Cardiovasc. Surg.* **13**, 301–319 (2001).
23. G. Buckberg, A. Mahajan, S. Saleh, J. I. Hoffman, C. Coghlan, Structure and function relationships of the helical ventricular myocardial band. *J. Thorac. Cardiovasc. Surg.* **136**, 578–589.e11 (2008).
24. M. Ballester, A. Ferreira, F. Carreras, The myocardial band. *Heart Fail. Clin.* **4**, 261–272 (2008).
25. G. Buckberg, J. I. E. Hoffman, A. Mahajan, S. Saleh, C. Coghlan, Cardiac mechanics revisited: The relationship of cardiac architecture to ventricular function. *Circulation* **118**, 2571–2587 (2008).
26. M. Mehdizadeh, J. Yang, Design strategies and applications of tissue bioadhesives. *Macromol. Biosci.* **13**, 271–288 (2013).
27. K. L. Mittal, *Progress in Adhesion and Adhesives* (Wiley, 2015).
28. H. Yoshida, K. Hirozane, A. Kamiya, Adhesive strength of autologous fibrin glue. *Biol. Pharm. Bull.* **23**, 313–317 (2011).
29. E. T. Roche, M. A. Horvath, I. Wamala, S. E. Song, W. Whyte, Z. Machaidze, N. V. Vasilyev, D. J. Mooney, F. A. Pigula, C. J. Walsh, Soft robotic sleeve supports heart function. *Sci. Transl. Med.* **9**, eaaf3925 (2017).
30. Y. L. Park, J. Santos, K. G. Galloway, E. C. Goldfield, R. J. Wood, A soft wearable robotic device for active knee motions using flat pneumatic artificial muscles, in *Proceedings of the 2014 IEEE International Conference on Robotics and Automation (ICRA 2014)*, pp. 4805–4810.
31. J. Wirekoh, Y. L. Park, Design of flat pneumatic artificial muscles. *Smart Mater. Struct.* **26**, 035009 (2017).
32. C. Pierpaoli, P. J. Basser, Toward a quantitative assessment of diffusion anisotropy. *Magn. Reson. Med.* **36**, 893–906 (1996).
33. R. R. Edelman, J. Gaa, V. J. Wedeen, E. Loh, J. M. Hare, P. Prasad, W. Li, In vivo measurement of water diffusion in the human heart. *Magn. Reson. Med.* **32**, 423–428 (1994).
34. T. G. Reese, R. M. Weisskoff, R. N. Smith, B. R. Rosen, R. E. Dinsmore, V. J. Wedeen, Imaging myocardial fiber architecture in vivo with magnetic resonance. *Magn. Reson. Med.* **34**, 786–791 (1995).
35. S. Ramadan, N. Paul, H. E. Naguib, Standardized static and dynamic evaluation of myocardial tissue properties. *Biomed. Mater.* **12**, 025013 (2017).
36. T. Shishido, M. Sugimachi, O. Kawaguchi, H. Miyano, T. Kawada, W. Matsura, Y. Ikeda, T. Sato, J. Alexander Jr., K. Sunagawa, A new method to measure regional myocardial time-varying elastance using minute vibration. *Am. J. Phys.* **274**, H1404–H1415 (1998).
37. R. Sherif, N. Hani, P. Narinder, Dynamic and static tensile mechanical properties of myocardial tissue. *Front. Bioeng. Biotechnol.* **4**, 00501 (2016).
38. Q. Liu, G. Nian, C. Yang, S. Qu, Z. Suo, Bonding dissimilar polymer networks in various manufacturing processes. *Nat. Commun.* **9**, 846 (2018).
39. N. Sheikh, A. A. Katbab, H. Mirzadeh, Isocyanate-terminated urethane prepolymer as bioadhesive base material: Synthesis and characterization. *Int. J. Adhes. Adhes.* **20**, 299–304 (2000).
40. D.-M. Drotlef, M. Amjadi, M. Yunusa, M. Sitti, Bioinspired composite microfibers for skin adhesion and signal amplification of wearable sensors. *Adv. Mater.* **29**, 1701353 (2017).
41. S. Port, S. Port, F. R. Cobb, R. E. Coleman, R. H. Jones, Effect of age on the response of the left ventricular ejection fraction to exercise. *N. Engl. J. Med.* **303**, 1133–1137 (1980).
42. L. Ricotti, B. Trimmer, A. W. Feinberg, R. Raman, K. K. Parker, R. Bashir, M. Sitti, S. Martel, P. Dario, A. Mencias, Biohybrid actuators for robotics: A review of devices actuated by living cells. *Sci. Robot.* **2**, eaag0495 (2017).
43. V. A. Webster-Wood, O. Akkus, U. A. Gurkan, H. J. Chiel, R. D. Quinn, Organismal engineering: Toward a robotic taxonomic key for devices using organic materials. *Sci. Robot.* **2**, eaap9281 (2017).
44. S.-J. Park, M. Gazzola, K. S. Park, V. Di Santo, E. L. Blevins, J. U. Lind, P. H. Campbell, S. Dauth, A. K. Capulli, F. S. Pasqualini, S. Ahn, A. Cho, H. Yuan, B. M. Maoz, R. Vijaykumar, J. W. Choi, K. Deisseroth, G. V. Lauder, L. Mahadevan, K. K. Parker, Phototactic guidance of a tissue-engineered soft-robotic ray. *Science* **353**, 158–162 (2016).
45. C. Nguyen, Z. Fan, Y. Xie, J. Pang, P. Speier, X. Bi, J. Kobashigawa, D. Li, In vivo diffusion-tensor MRI of the human heart on a 3 tesla clinical scanner: An optimized second order (M2) motion compensated diffusion-preparation approach. *Magn. Reson. Med.* **76**, 1354–1363 (2016).
46. C. T. Nguyen, J. Dawkins, X. Bi, E. Marbán, D. Li, Diffusion tensor cardiac magnetic resonance reveals exosomes from cardiosphere-derived cells preserve myocardial fiber architecture after myocardial infarction. *JACC Basic Transl. Sci.* **3**, 97–109 (2018).
47. D. H. MacIver, R. S. Stephenson, B. Jensen, P. Agger, D. Sánchez-Quintana, J. C. Jarvis, J. B. Partridge, R. H. Anderson, The end of the unique myocardial band: Part I. Anatomical considerations. *Eur. J. Cardiothorac. Surg.* **53**, 112–119 (2018).
48. J. I. E. Hoffman, Will the real ventricular architecture please stand up? *Phys. Rep.* **5**, e13404 (2017).
49. D. H. MacIver, J. B. Partridge, P. Agger, R. S. Stephenson, B. J. D. Boukens, C. Omann, J. C. Jarvis, H. Zhang, The end of the unique myocardial band: Part II. Clinical and functional considerations. *Eur. J. Cardiothorac. Surg.* **53**, 120–128 (2018).
50. J. Lessick, E. Ghersin, S. Abadi, S. Yalonetsky, Accuracy of the long-axis area-length method for the measurement of left ventricular volumes and ejection fraction using multidetector computed tomography. *Can. J. Cardiol.* **24**, 685–689 (2008).
51. S. Mori, B. J. Crain, V. P. Chacko, P. C. M. Van Zijl, Three-dimensional tracking of axonal projections in the brain by magnetic resonance imaging. *Ann. Neurol.* **45**, 265–269 (1999).
52. Y. Fan, W. Ronan, I. Teh, J. E. Schneider, C. E. Varela, W. Whyte, P. McHugh, S. Leen, E. T. Roche, A comparison of two quasi-static computational models for assessment of intra-myocardial injection as a therapeutic strategy for heart failure. *Int. J. Numer. Methods Biomed. Eng.* **35**, e3213 (2019).

Acknowledgments: We thank A. Greer for illustration, S. Hua for initial help with actuator fabrication, J. Weaver for help with the microCT imaging, and A. F. Corno for reviewing and editing the manuscript. **Funding:** Funding was from the Mechanical Engineering Department at the Massachusetts Institute of Technology, the Institute for Medical Engineering and Science at the Massachusetts Institute of Technology, and NSF CAREER award no. 1847541. Additional funding was from the Massachusetts General Hospital Cardiovascular Research Center and Martinos Center for Biomedical Imaging (NIH R21EB024701), NSF EFRI award no. 1935291: C3 SoRo: Functional-Domain Soft Robots (FunDo SoRo) Precisely Controlled by Quantitative Dynamic Models and Data, and a Charles H. Hood Award for Excellence in Child Health. **Author contributions:** C.P., N.V.V., C.T.N., and E.T.R. designed the research. C.P. manufactured the biohybrid heart and the biorobotic hybrid heart. C.P., G.H., and A.R. conducted the actuator experiments. C.P., Y.F., and C.T.N. conducted the DT-MRI imaging. H.Y. and X.Z. made the TissueSil adhesive. M. Singh, C.P., and A.R. conducted adhesive testing. Y.F. and G.H. conducted the FE simulations. M. Saeed performed echocardiography. C.P., Y.F., G.H., M. Singh, A.R., X.Z., T.W.J.S., C.T.N., and E.T.R. analyzed the data. C.P., Y.F., G.H., M. Singh, and E.T.R. wrote the manuscript. **Competing interests:** U.S. Patent application pending filed by the Massachusetts Institute of Technology. E.T.R. is a consultant for and has equity in Holistic Medical. **Data and materials availability:** All data needed to evaluate the conclusions in the paper are present in the paper or the Supplementary Materials. The heart model is available with a materials transfer agreement.

Submitted 29 July 2019

Accepted 8 January 2020

Published 29 January 2020

10.1126/scirobotics.aay9106

Citation: C. Park, Y. Fan, G. Hager, H. Yuk, M. Singh, A. Rojas, A. Hameed, M. Saeed, N. V. Vasilyev, T. W. J. Steele, X. Zhao, C. T. Nguyen, E. T. Roche, An organosynthetic dynamic heart model with enhanced biomimicry guided by cardiac diffusion tensor imaging. *Sci Robot.* **5**, eaay9106 (2020).

An organosynthetic dynamic heart model with enhanced biomimicry guided by cardiac diffusion tensor imaging

Clara Park, Yiling Fan, Gregor Hager, Hyunwoo Yuk, Manisha Singh, Allison Rojas, Aamir Hameed, Mossab Saeed, Nikolay V. Vasilyev, Terry W. J. Steele, Xuanhe Zhao, Christopher T. Nguyen and Ellen T. Roche

Sci. Robotics **5**, eaay9106.

DOI: 10.1126/scirobotics.aay9106

ARTICLE TOOLS

<http://robotics.sciencemag.org/content/5/38/eaay9106>

SUPPLEMENTARY MATERIALS

<http://robotics.sciencemag.org/content/suppl/2020/01/27/5.38.eaay9106.DC1>

REFERENCES

This article cites 48 articles, 4 of which you can access for free
<http://robotics.sciencemag.org/content/5/38/eaay9106#BIBL>

PERMISSIONS

<http://www.sciencemag.org/help/reprints-and-permissions>

Use of this article is subject to the [Terms of Service](#)

Science Robotics (ISSN 2470-9476) is published by the American Association for the Advancement of Science, 1200 New York Avenue NW, Washington, DC 20005. The title *Science Robotics* is a registered trademark of AAAS.

Copyright © 2020 The Authors, some rights reserved; exclusive licensee American Association for the Advancement of Science. No claim to original U.S. Government Works

Supplementary Materials for

An organosynthetic dynamic heart model with enhanced biomimicry guided by cardiac diffusion tensor imaging

Clara Park, Yiling Fan, Gregor Hager, Hyunwoo Yuk, Manisha Singh, Allison Rojas, Aamir Hameed, Mossab Saeed, Nikolay V. Vasilyev, Terry W. J. Steele, Xuanhe Zhao, Christopher T. Nguyen*, Ellen T. Roche*

*Corresponding author. Email: christopher.nguyen@mgh.harvard.edu (C.T.N.); etr@mit.edu (E.T.R.)

Published 29 January 2020, *Sci. Robot.* **5**, eaay9106 (2020)
DOI: 10.1126/scirobotics.aay9106

The PDF file includes:

Fig. S1. TissueSil bonding chemistry and penetration to microstructures.
Fig. S2. Fabrication steps for the flat soft robotic matrix.
Fig. S3. Uniaxial tensile testing of fresh versus synthetic myocardium.
Fig. S4. Cyclic fatigue testing on fixed tissue-adhesive composite.
Fig. S5. Construction of DT-MRI-based FE model of the left ventricle.
Fig. S6. A comparison of cardiac parameters of the biorobotic hybrid heart model with in vivo and in silico heart models.

Other Supplementary Material for this manuscript includes the following:

(available at robotics.sciencemag.org/cgi/content/full/5/38/eaay9106/DC1)

Movie S1 (.mp4 format). Tissue-adhesive failure during uniaxial tensile testing.
Movie S2 (.avi format). Dissection of HVMB.
Movie S3 (.mp4 format). The structure of the biorobotic hybrid heart under MRI.
Movie S4 (.avi format). Visualization of the biorobotic hybrid heart actuation under GRE CINE MRI.
Movie S5 (.mp4 format). Motion of the biorobotic hybrid heart and its reference in vivo porcine heart under echocardiography.

Supplementary Figures

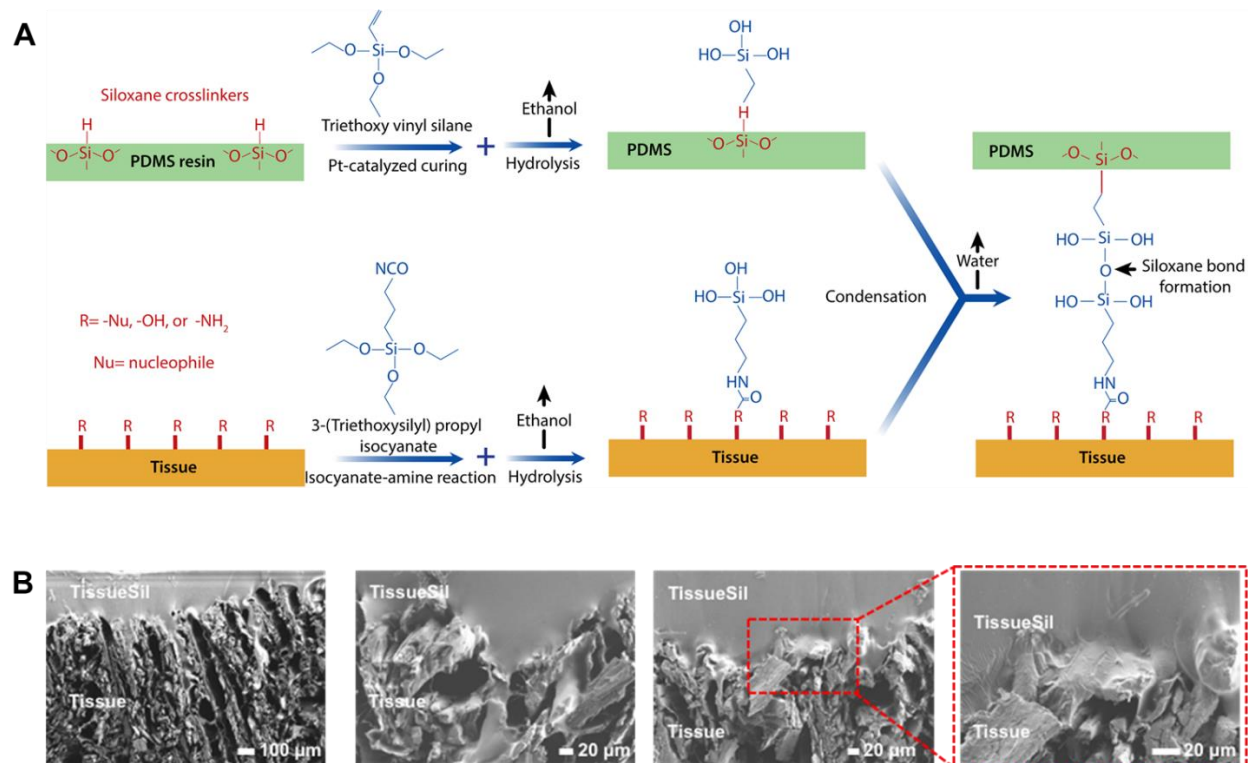


Figure S1. TissueSil bonding chemistry and penetration to microstructures. (A) Schematic of TissueSil Chemistry. **(B)** Uncolored SEM images of TissueSil applied onto rough myocardial tissue surface in Fig. 3A.

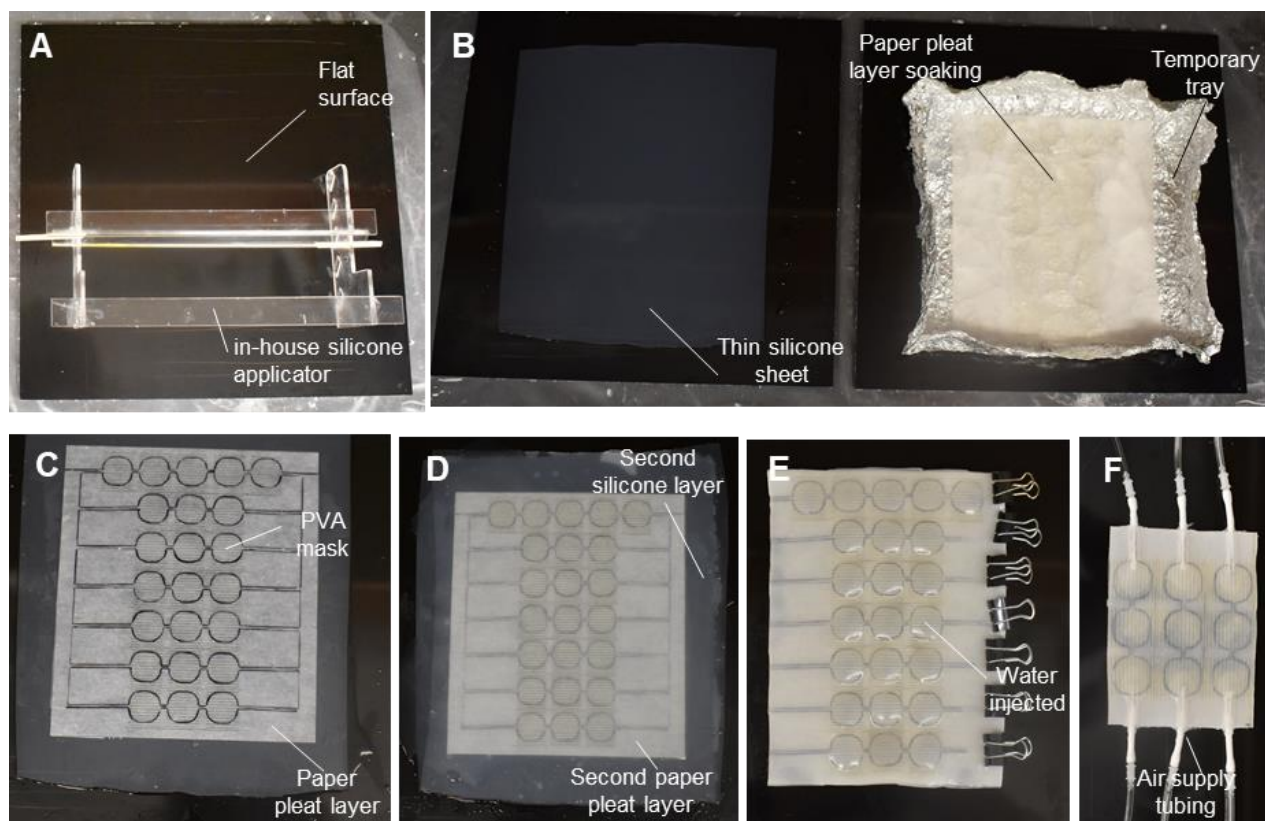


Figure S2. Fabrication steps for the flat soft robotic matrix. (A) A custom-made silicone applicator for fabricating thin silicone sheets of defined heights. The apparatus is rolled over pre-cured silicone, and the height of the transverse section defines the thickness of the layer. (B) A pre-fabricated 1.2 mm thickness silicone sheet (left) and the paper pleat layer soaking in uncured silicone in a tray (right). (C) Partial assembly of the actuator layers. The PVA bladder layer marked with pen around the edges is placed on top of the pre-soaked paper pleat layer and the cured silicone sheet. (D) Full assembly with second paper pleat layer and silicone sheet placed on top of (C). (E) Trimmed actuator assembly post-curing and PVA bladder layer dissolving in water. (F) Final actuator matrix after removing dissolved PVA and inserting air supply tubing.

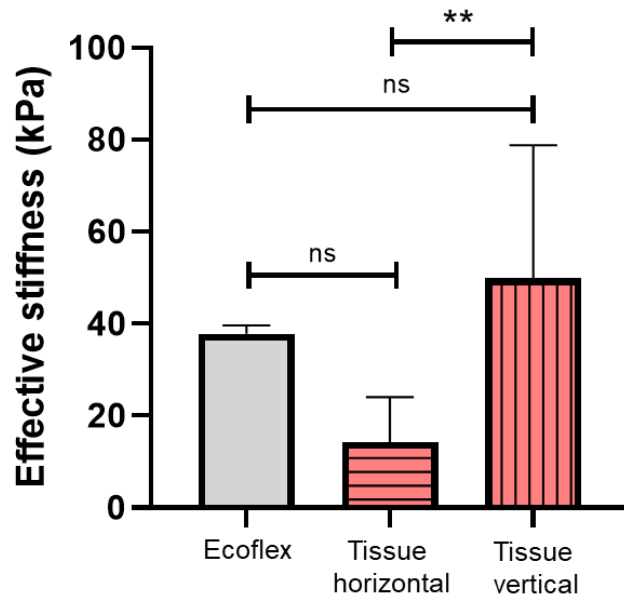


Figure S3. Uniaxial tensile testing of fresh versus synthetic myocardium. Young's modulus of synthetic myocardium made from a soft elastomeric matrix, Ecoflex 00-20, ($n = 5$) is compared to fresh myocardial tissue stretched across (horizontal) ($n = 7$) and along (vertical) ($n = 8$) the fiber direction. Data are presented as mean \pm SD. One-way ANOVA with Tukey post hoc correction was used to compare the groups. ** $p < 0.01$.

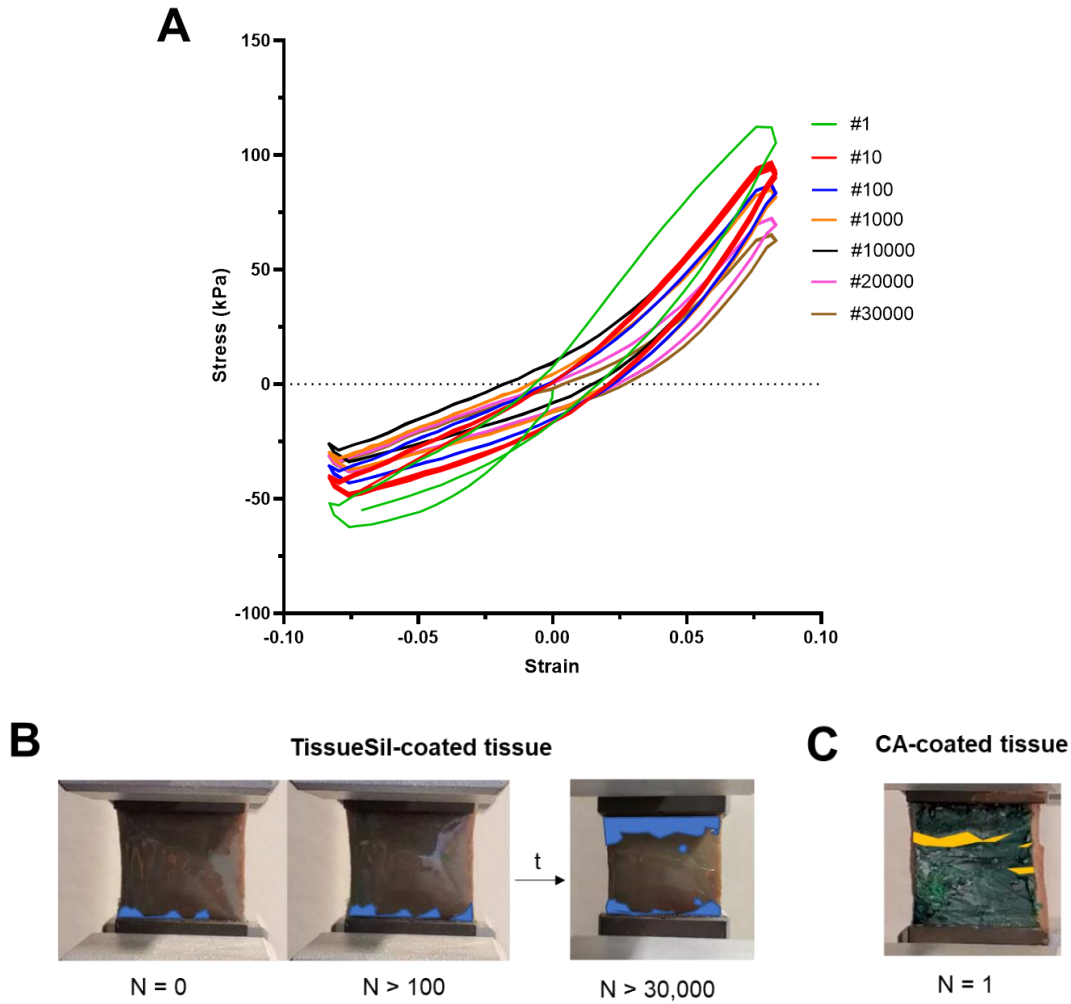


Figure S4. Cyclic fatigue testing on fixed tissue-adhesive composite. Tension-compression cyclical strain loading of $\pm 1.66\text{mm}$ (or 8.3%) at 1 Hz for up to 30,000 cycles with triangular waveforms at ambient temperature. **(A)** Hysteresis loop of tissue-TissueSil composite over number of cycles. **(B)** Visual images of tissue-adhesive failures. Left) Tissue-TissueSil composite over time, showing the slow progression of failure. At the start of the test, there was a small area of delamination, 2.4% of total bonding area ($N = 0$) to 4.5% ($N > 100$). The delamination area was approximately 16.3% when the test was terminated ($N > 30,000$). Areas of adhesive delamination are shown in blue. **(C)** Tissue-cyanoacrylate composite showing immediate adhesive failure at the 1st cycle. Delaminated or cracked adhesive is shown in yellow. N = number of cycles.

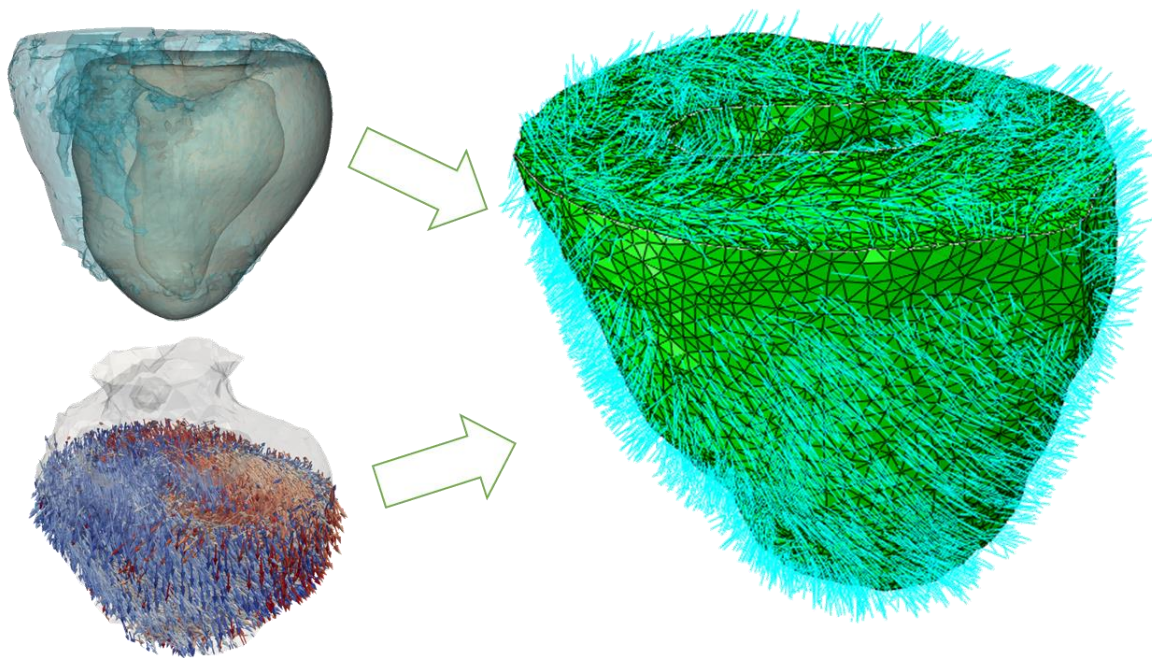


Figure S5. Construction of DT-MRI-based FE model of the left ventricle. Schematic of the segmentation of the LV of an intact 3D porcine heart using Mimics (top left) and mapping of principal diffusion directions (bottom left) obtained from DT-MRI onto a finite element mesh (right).

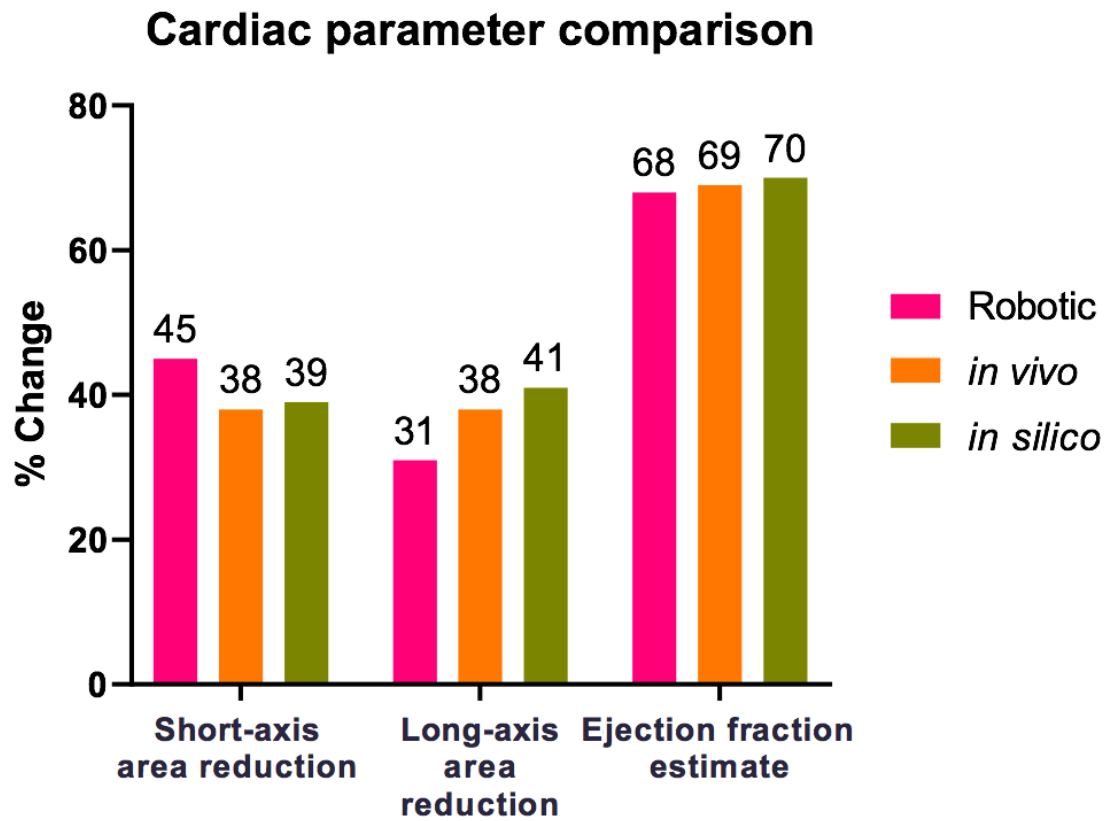


Figure S6. A comparison of cardiac parameters of the biorobotic hybrid heart model with *in vivo* and *in silico* heart models. Left ventricular area reduction in the short-axis plane, left ventricular area reduction in the long-axis plane, and estimated ejection fraction for the biorobotic hybrid heart, *in vivo* porcine heart motion under echocardiography, and the predicted motion from the *in silico* FE model.